LOCAL ATOMIC STRUCTURE IN Al-RE MARGINAL METALLIC GLASSES

A THESIS SUBMITTED TO
THE GRADUATE SCHOOL OF NATURAL AND APPLIED SCIENCES
OF
MIDDLE EAST TECHNICAL UNIVERSITY

BY

MERT ÖVÜN

IN PARTIAL FULFILLMENT OF THE REQUIREMENTS
FOR
THE DEGREE OF MASTER OF SCIENCE
IN
METALLURGICAL AND MATERIALS ENGINEERING

JUNE 2016

Approval of the thesis:

LOCAL ATOMIC STRUCTURE IN Al-RE MARGINAL METALLIC GLASSES

submitted by **MERT ÖVÜN** in partial fulfillment of the requirements for the degree of **Master of Science in Metallurgical and Materials Engineering Department, Middle East Technical University** by,

Prof. Dr. Gülbin Dural Ünver _____
Dean, Graduate School of **Natural and Applied Science**

Prof. Dr. C. Hakan Gür _____
Head of Department, **Metallurgical and Materials Engineering**

Assoc. Prof. Dr. Yunus Eren KALAY _____
Supervisor, **Metallurgical and Materials Eng. Dept., METU**

Examining Committee Members:

Prof. Dr. Tayfur Öztürk _____
Metallurgical and Materials Engineering Dept., METU

Assoc. Prof. Dr. Yunus Eren KALAY _____
Metallurgical and Materials Engineering Dept., METU

Prof. Dr. Kadri Aydınol _____
Metallurgical and Materials Engineering Dept., METU

Assist. Prof. Dr. Mert Efe _____
Metallurgical and Materials Engineering Dept., METU

Assist. Prof. Dr. Caner Şimşir _____
Manufacturing Engineering Dept.., ATILIM UNIVERSITY

Date: 07.06.2016

I hereby declare that all information in this document has been obtained and presented in accordance with academic rules and ethical conduct. I also declare that, as required by these rules and conduct, I have fully cited and referenced all material and results that are not original to this work.

Name, Last name: Mert Övün

Signature :

ABSTRACT

LOCAL ATOMIC STRUCTURE IN Al-RE MARGINAL METALLIC GLASSES

Övün, Mert

M.S., Department of Metallurgical and Materials Engineering

Supervisor: Assoc. Prof. Dr. Yunus Eren KALAY

June 2016, 84 pages

Partial devitrification of the Al-RE marginal metallic glasses results in anomalous nucleation rate of nanocrystals conflicting with the classical nucleation theory by several orders of magnitude. One of the theoretical approaches explaining this phenomenon is the medium-range order (MRO) structures within the range of 1-2 nm that may be present both in the quenched amorphous state and its liquid precursor. In this work, these structures have been investigated conducting both experimental methods such as high energy X-ray diffraction (HEXRD) using synchrotron radiation, and computational methods as molecular dynamics (MD) , Monte Carlo (MC) and reverse Monte Carlo (RMC) simulation techniques. In order to make molecular simulations, interatomic potentials based on diffraction experiments have been developed. This work was partially supported by the Scientific and Technological Research council of Turkey (TÜBİTAK) under Grant No. 113M346.

Keywords: Monte Carlo simulations, medium-range ordering, phase separation, chemical and topological configuration, Al-RE metallic glass

ÖZ

Al-RE BAZLI METALİK CAMLARDA LOKAL ATOMİK YAPI

Övün, Mert

Yüksel Lisans, Metalurji ve Malzeme Mühendisliği Bölümü

Tez Yöneticisi: Doç. Dr. Yunus Eren KALAY

Haziran 2016, 84 sayfa

Al-RE bazlı metalik camların kısmi kristalendirilmesi, klasik çekirdeklenme teorisiyle çelişen bir şekilde, anormal miktarlarda nanokristal oluşumuyla sonuçlanmaktadır. Bu olguyu teorik düzlemde açıklayan bir yaklaşım olarak amorf ve sıvı fazlarda 1-2 nm boyutlarında orta-menzilli düzenli yapıların varlığı önerilmektedir. Bu çalışmada, bu yapılar hem geçirimli elektron mikroskobu yüksek enerjili X-ray kırınımı gibi deneysel metodlar hem de moleküler dinamik, Monte Carlo ve ters Monte Carlo gibi simülasyon yöntemleri kullanılarak araştırılmıştır. Moleküler simülasyonları yapmak için deneysel kırınım verilerini temel alan interatomik potansiyeller geliştirilmiştir. Bu tez çalışması kısmi olarak Türkiye Bilimsel ve Teknolojik Araştırma Kurumu (TÜBİTAK) tarafından (Proje No: 113M346) desteklenmiştir.

Anahtar Kelimeler: Monte Carlo simülasyonları, orta-menzilli düzenlenme, faz ayrışması, kimyasal ve topolojik konfigürasyon, Al-RE metalik cam

To My Beloved Family

ACKNOWLEDGEMENTS

I am highly grateful and obliged to my supervisor Assoc. Prof. Y. Eren Kalay for his guidance, patience and continuous encouragement throughout my graduate study.

I am also very grateful to my previous and current laboratory partners Anıl Kantarcıoğlu, Tuba Demirtaş, Can Yıldırım, Mertcan Başkan, Eyüp Can Demir, Serkan Yılmaz, Ayşe Merve Genç Ünalan, Özgün Acar, Mustafacan Kutsal, Bengisu Yaşar and Fatih Sıkan for their motivation and huge support.

I owe my deepest thanks to my lifelong friends Burcu, Tekin, Faruk, Ulaş and Deniz for being there whenever I need, for their constant intellectual stimulation, and for the provocation to learn and to live.

Finally, I would like to thank to my parents for their love and concern throughout my life. Especially, I would like to express my heart-felt gratitude to my mother, Derya Övün for her never ending support and patience. This accomplishment would not have been possible without her.

TABLE OF CONTENTS

LIST OF TABLES

TABLES

LIST OF FIGURES

FIGURES

CHAPTER 1

INTRODUCTION

1.1 Overview of Metallic Glasses

Unlike ionic and covalent species, metals and their alloys tend to have crystalline atomic structure in their solid state due to directionless nature of their metallic bonding which enables the atoms to rearrange into the lowest energy configuration by following minimal bonding and angular constraints. Crystallization proceeds several orders of magnitude faster in metallic systems as compared to traditional non-crystalline systems, and it requires the combination of particularly rare compositions and special production techniques to bypass the crystallization. As a result, the development of metallic glasses had been waited until the second half of the twentieth century, despite the non-crystalline solid materials, namely glasses, have been employed throughout the history of civilization.

In 1960, Duwez et. al. [1] produced the first metallic glass alloy, $Au_{75}Si_{25}$, as a thin foil specimen by rapid quenching from melt with a cooling rate on the order of 10^6 K/s. The produced glassy structure was highly unstable, so that metastable crystalline phases were detected within 24 hours after the production, at room temperature. After that point, development of metallic glasses have continued with an increasing speed. Today, thousands of metallic glass alloys have been produced with the intention of creating various types of engineering attributes which would not be satisfied by other classes of materials. These attributes are due to unique interatomic arrangements and interactions within metallic glasses. Metallic glasses are often classified according to their constituent elements as follows [2]. The candidate elements in the periodic table are divided into six categories: alkali and alkaline metals in groups IA and IIA (Mg,

Ca, Be), semi- or simple metals in IIIA and IVA groups neighboring the semiconductors (Al, Ga), early transition metals in groups IVB to VIIB (Ti, Zr, Hf, Nb, Ta, Cr, Mo, Mn), late transition metals in groups VIIIB, IB and IIB (Fe, Co, Ni, Cu, Pd, Pt, Ag, Au, Zn), rare-earth metals (Sc, Y, La, Ce, Sm, Tb etc.), non-metals and metalloids (B, C, P, Si, Ge). Metallic glasses are typically constituted by the elements from at least two different groups described above, and they can also be classified according to these groups of elements.

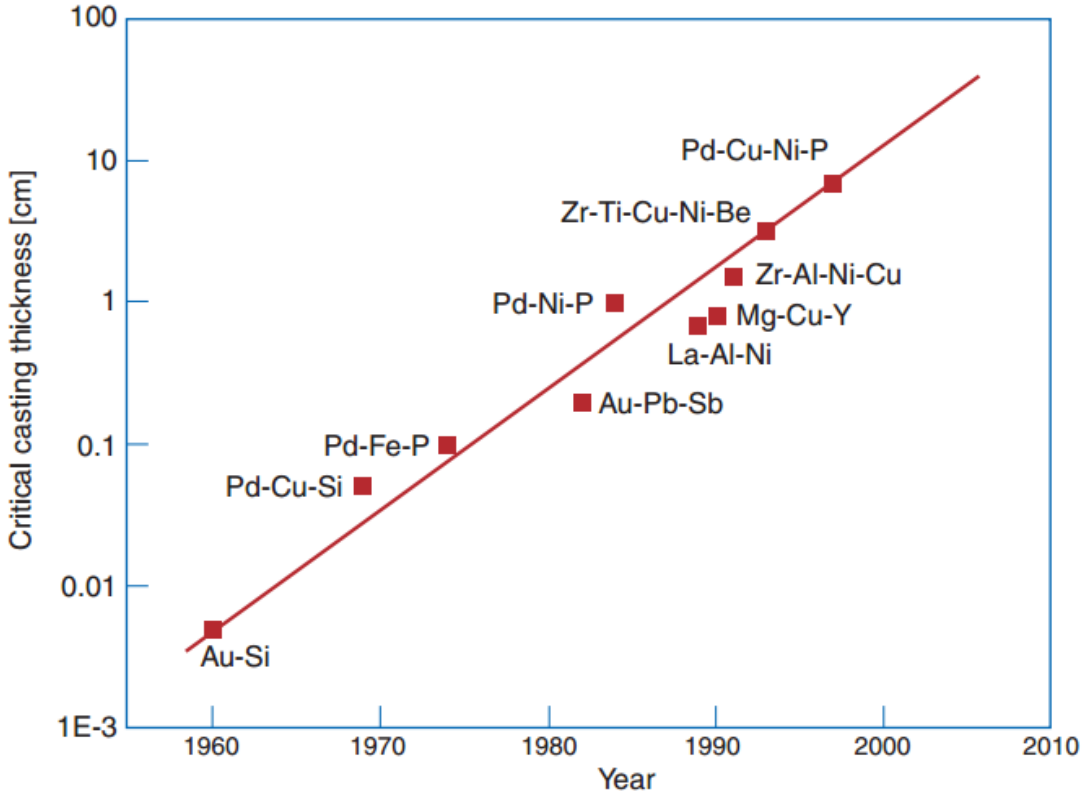

Figure 1.1 The critical casting thickness versus the year in which alloys were discovered. Adopted from [3].

However, interesting features that this brand new type of materials presents are not single-handedly enough for most of engineering practices. The main challenge for metallic glasses is the difficulty in producing them in wide dimensional ranges because of the challenges in controlling the cooling rate all over the piece, particularly for large-size specimens. Therefore, the ability to bypass nucleation, which is commonly called

glass forming ability (GFA), should continuously be improved for practical applications. There are various suggestions to parameterize GFA having both thermodynamic and atomistic bases, which will be discussed later. However, one of the most relevant engineering measures of the ability for glass formation is the critical casting thickness, which is the maximum thickness of an alloy specimen that can be produced without crystallization. Figure 1.1 shows the historical development of metallic glasses in terms of critical casting thickness which has been improved by more than three orders of magnitude within four decades [3].

The theory for increasing the glass forming ability and thermal stability has been improved in terms of both thermodynamic and atomistic approaches, and critical cooling rates for glass formation have dropped correspondingly from 10^6 K/s to 1-100 K/s, which is similar to these of oxide glasses. In order to enhance GFA, Inoue [4] has proposed an empirical rule such that more than three constituent elements with large atomic size ratios above 12% and negative heats of mixing are necessary. This approach provides an increase in the degree of dense random packing structure, hence, the long-range atomic rearrangement that is necessary for crystallization becomes difficult. At the same time, novel production methods have been developed allowing the production of samples with higher dimensions at higher scales which are convenient for engineering applications. After all, resulting amorphous metals with relatively high GPA with thickness of several milimeters are termed as bulk metallic glasses (BMG).

Some metallic glass-forming alloys, on the other hand, have quite different properties as compared to BMGs. These glasses, which are called marginal metallic glasses (MMG), exhibit peculiar characteristics in various aspects exceeding the limits of theoretical foundations of the phenomena of glass transition and even nucleation [5]. While BMGs possess the strongest glass forming ability near eutectic compositions, Al-based MMGs are able to form glass phase at the compositions significantly further than the eutectic point. Composition ranges for glass formation and eutectic points of several Al-based marginal metallic glass systems were shown in Figure 1.2. Secondly,

the glass transition temperature peak is obscured by the first crystallization peak in DSC experiments of these alloys [6]. Moreover, temperature regions where the phase transformations occur is relatively much more sensitive to heating rate. As the glass transformation is immediately followed by crystallization during devitrification, probing the supercooled liquid region is experimentally inaccessible. Therefore, the origin of dynamic behavior of MMGs such as liquid fragility remains hidden.

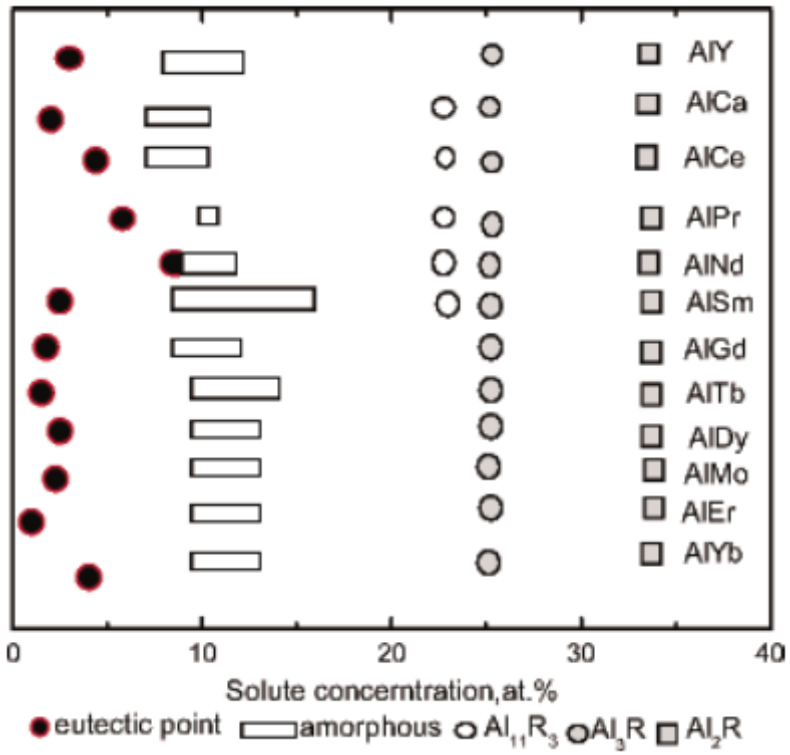

Figure 1.2 Composition ranges for the formation of an amorphous phase in Al-based MMG systems. Adopted from [5]

Devitrification of Al-based MMGs results in formation of very high number densities of primary fcc-Al nanocrystals (10^{21}–10^{24} m^{-3}), and the nucleation number density of such order of magnitude cannot be explained by the classical nucleation theory (CNT) [7]. The resulting nanocrystalline microstructure is regarded as a promising engineering materials with a variety of application areas. Besides, this enigmatic behavior is directly a challenging question of basic science, including various

unclearified topics of condensed matter physics such as nucleation and glass transition. The solution to this intriguing problem is thought to be hidden within the atomistic structure and dynamics of the supercooled liquid which is out of reach of any experimental observation.

1.2 Properties and Potential Applications of Metallic Glasses

The science and technology of metallic glasses is still considered to be in its adolescence. Having quite interesting and promising properties as their combination is unique to this class of materials, they are unsatisfactory for industrial realization in a lot of aspects that need to be ameliorated [8].

The cost of components and processing is relatively high within today's capabilities. The requirement of high cooling rates brings the necessity of special casting instruments. Additionally, some production methods such as vacuum die-casting is relatively slow leading to infeasible production rates. Temperatures above the crystallization temperature, the use and processing is limited due to instability. Moreover, plastic flow that is localized at shear bands results in very low ductility, especially in tension with the exception of a few alloy compositions. Therefore, they can be easily embrittled by applying force or changing the temperature. These characteristics limit the use of metallic glasses in terms of processing and application.

Furthermore, the research and development process of novel metallic glass alloys with decent practically is also difficult, slow and expensive. This is mainly because, glass forming ability requirement that is necessary to obtain the material itself as amorphous highly constraints possible composition ranges; therefore, tuning the material properties by changing the compositional parameters is hard to even impossible in many cases.

Despite the abovementioned disadvantages, metallic glasses are utilized as to be used in key component parts and high-end products even today due to their unique properties. Microstructural features such as grain and phase boundaries are absent and related compositional inhomogeneities are minimum. There are no conventional

crystalline defects such as dislocations etc.; since, there is no crystalline structure at all. Therefore, metallic glasses can possess unordinary mechanical properties such as high yield strength, high specific strength, high resilience per unit volume and mass, high hardness, giving good wear resistance, high corrosion resistance, and high magnetic permeability [9]. Electrical resistance is almost independent to temperature. There are even some biocompatible alloy compositions. Despite the disadvantages, there are also some processing advantages such as low solidification shrinkage and lack of grain structure allows high precision and finish in castings. For some alloys there is a considerable gap between glass transition temperature and crystallization temperature in which the glass can be formed as a supercooled liquid having high viscosity and low strain-rate sensitivity.

High hardness and corrosion resistance makes metallic glasses suitable for tools such as knife edges. High resilience enables the use of metallic glasses for springs and sport-specific materials such as tennis rackets and golf clubs requiring high elastic energy storage per unit mass and volume. Metallic glasses can also be deposited as thin films for the use of fashion items such as watch cases, mobile phone cases etc. Thin film deposition can also be used in the production of MEMS devices.

1.3 Thermodynamics and Kinetics

The glass formation is a result of of two distinct processes competing with each other: Glass transition and nucleation. In this section, thermodynamic and kinetic aspects of these two phenomena was briefly summarized.

1.3.1 The Glass Transition

Glass transformation is the rapid dynamic slowdown of the disordered liquid such that it behaves like a solid as the temperature decreases, due to a dramatic increase in the system relaxation time. There is little agreement on why this type of dynamic arrest occurs; since there is no significant structural change accompanying this behavior. Glass transformation is characterized by several thermodynamic and kinetic aspects

and it is classified as a second order phase transition due to its characteristic features [10].

Typically volume of a liquid metal decreases with decreasing temperature up to freezing point, depending on its thermal expansion coefficient. During freezing a sudden drop in the specific volume occurs as the liquid structure transforms into crystalline solid. However, crystallization can be retarded or bypassed completely due to thermodynamic and kinetic characteristics of the process of nucleation. Therefore, the liquid can be undercooled below thermodynamically stable freezing point without undergoing any phase transformation. The degree of undercooling that can be obtained without crystallization depends of several parameters such as temperature dependence of viscosity of the liquid, interfacial energy between liquid and competing stable/metastable crystalline phases, and bulk free energy between liquid and the crystalline phases. For glass-forming liquids in which these parameters have optimal values, at some temperature well below the melting point the undercooled liquid may transform into solid glass. This point is called as the point of glass transformation.

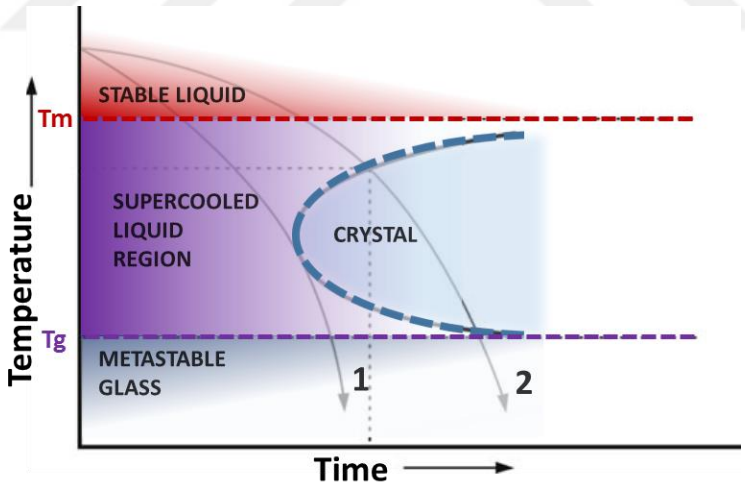

Figure 1.3 The TTT diagram of a hypothetical glass-forming alloy with an example cooling path having critical rate of cooling (as shown in path 1).

For a specified glass-forming alloy composition the abovementioned parameters are suitable so that the crystallization below melting temperature is a relatively slow

process. Even though it can be bypassed by continuous cooling at a rate that should be faster than some value which is called critical cooling rate. In Figure 1.3, TTT diagram of a hypothetical alloy is shown. First cooling path represents the critical cooling rate at which the glass can be formed.

While the change in specific volume is sudden during crystallization, it is continuous in glass transformation, as a second order phase transformation. As shown in Figure 1.4, the temperature of glass transformation can be determined as a sudden change in the slope of specific volume vs. temperature plot representing the change in the coefficient of thermal expansion. It is also observed that the glass transformation temperature depends on cooling rate.

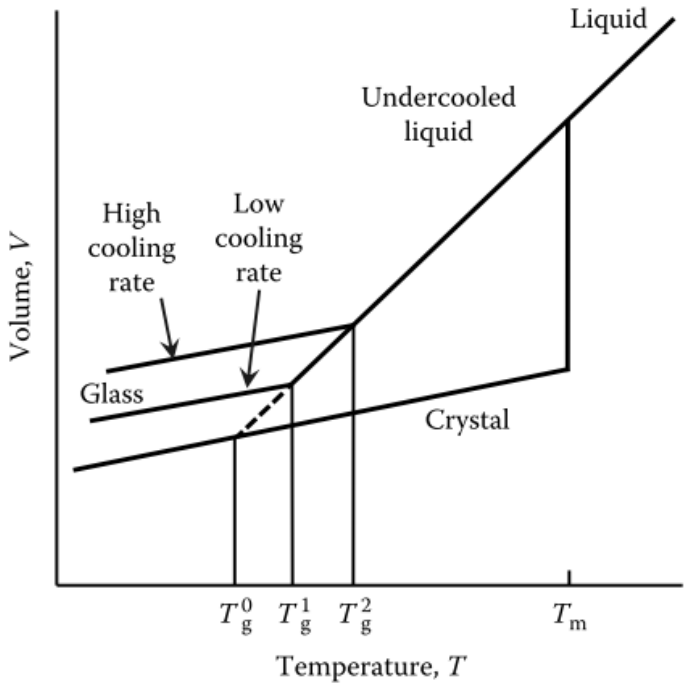

Figure 1.4 The change in volume with temperature during crystallization and glass transformation. Adopted from [10]

The temperature dependence of entropy exhibits a similar behavior to that of volume. While entropy suddenly decreases at crystallization and become relatively steady after crystallization at lower temperatures as in the case for specific volume, it keeps

decreasing at a similar rate in undercooled liquid phase as if it would intersect the plot for the crystallization scenario at some temperature called as Kauzmann temperature; the temperature at which entropy of liquid become equal to entropy of crystal. Below that temperature the entropy of glass is lower that of liquid, and more interestingly, this behavior implies that the entropy may drop to negative which is impossible or rather meaningless (entropy crisis). This situation is known as Kauzmann paradox [11]. Although there are some other resolutions to the paradox such as a smooth decrease in the heat capacity near Kauzmann temperature or a sharp decrease in the heat capacity by another liquid-liquid phase transition, it is commonly stated that the liquid must undergo glass transition (or crystallization) at some point above Kauzmann temperature.

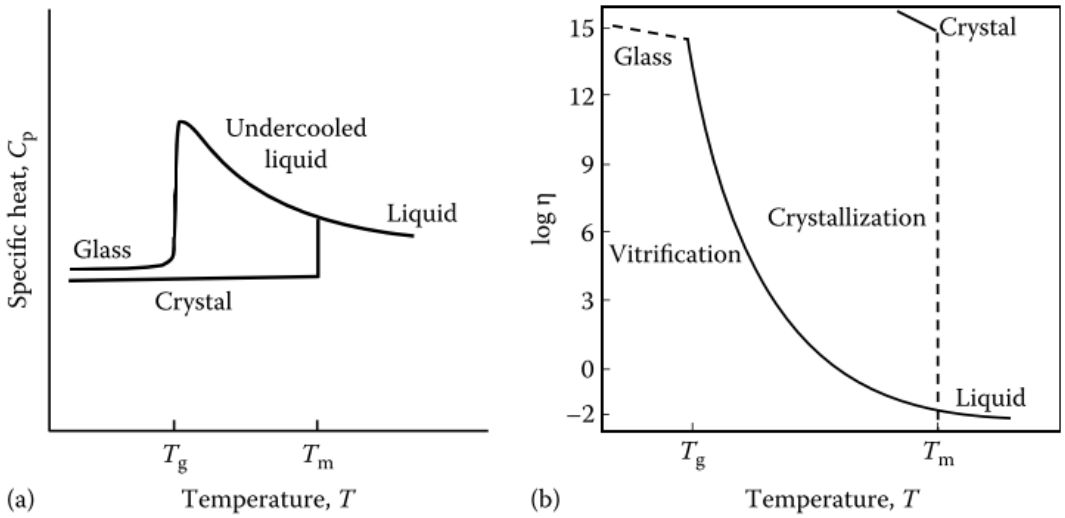

Figure 1.5 Variation of (a) specific heat and (b) viscosity for crystal and glass formation. Adopted from [10]

The change in specific heat capacity and viscosity with temperature is shown in Figure 1.5. The heat capacity of undercooled liquid increases with decreasing temperature and the difference in heat capacity between the undercooled liquid and glass is increased as the system approaches the glass transition. At glass transition, the heat capacity drops suddenly, and reaches the value which is very close to that of crystal.

While during crystallization from liquid viscosity increases suddenly about 15 orders of magnitude, the increase of viscosity with decreasing temperature is continuous for all glass forming alloys. Conventionally, the temperature dependence of viscosity in glasses shows Arrhenius behavior. These type of glass-forming liquids are called strong. However, in some liquids there are deviations from the Arrhenius behavior. As this deviation increases, the liquid is called more fragile. This deviation is ascribed to some atomistic dynamic processes within the liquid, which will be explained later.

For an ideal strong liquid the Arrhenius relation between viscosity and temperature is as below:

$$\eta = \eta_0 \exp(E/k_B T) \qquad (1.1)$$

proposing a linear relationship between $\log \eta$ and $1/T$; where η_0 is the pre-exponential factor limiting the change in viscosity at high-temperatures in liquid, E is the activation energy, and k_B is the Boltzmann constant [12]. Fragile liquids exhibit a more pronounced kinetic slow-down which is commonly described by the Vogel-Tammann-Fulcher (VTF) equation [13]–[15]:

$$\eta = A \exp[B/(T - T_0)] \qquad (1.2)$$

where A has at most a weak temperature dependence, and B and T_0 are temperature-independent constants. The deviation from Arrhenius behavior, in other words, degree of fragility is related to the dimensionless quantity B/T_0 and the strongest glass-former liquid (ideally Arrhenius behavior) is observed where T_0 equals to zero. VTF equation provides a successful fit for experimentally observer viscosity values and T_0 term is determined by the resulting fit. Interestingly enough, although T_0 is a kinetic parameter determining the viscosity change with temperature, and Kauzmann temperature (T_K) is a thermodynamic parameter of the system that is related to the entropy crisis; experimentally found T_0 values are very close to T_K of these systems, which may imply a non-coincidental behavior [16].

1.3.2 Nucleation

Unlike second-order phase transitions, first-order phase transitions are described by the discontinuity of the free energy curve with respect to other thermodynamic variables such as temperature and pressure. Corresponding experimental quantities, entropy and volume, exhibit a sudden change as the parent phase transforms into its children as described in previous sections. First-order phase transformation is also characteristically identified by the co-existence of two (or more) phases in a non-equilibrium thermodynamic state. One of these phases is the metastable parent (for example, liquid or glass as in the case of solidification or vitrification), the other is the stable daughter phase at given thermodynamic conditions. [17] The co-existence of such multiple phases also implies the initiation and the survival of an interface between them. The formation of the daughter phase that is bound by its interface is called *nucleation*.

Nucleation is at the central point of many occurrences in our world, and it has a critical importance in understanding a wide spectrum of phenomena. For example, the mechanisms of global warming, such as the effects of atmospheric aerosols on the formation of water droplets and ice crystals, have been investigated through the perspective of nucleation and phase transitions [18]. Another example is that there is huge amount of interest in the cryopreservation of living tissues via bypassing the nucleation of ice for biological and medical applications [19]. Finally, the kinetics of transformation and replication cycles of energy-harnessing prebiotics on the surface of supersaturated inorganic species at sea-floor hydrothermal vents in the lifeless earth (just as in today) is being understood through the theories of nucleation [20] which may elucidate the origin of life in earth [21] and evaluate the possibilities of it at extraterrestrial environments [22].

When a phase is put into a non-equilibrium condition, by driving the system out of the stability region of the phase via changing temperature, pressure, composition and/or some other parameter that would provide a sufficient change in the chemical potential of the system, the phase would initially reside in a local minimum on the free energy

surface (*metastable* state), which is relatively stable to some thermodynamic fluctuations; however, this phase should will eventually evolve into another phase that corresponds to the global minimum of the energy surface, which is the *stable* state (Fig. 1.6) [17].

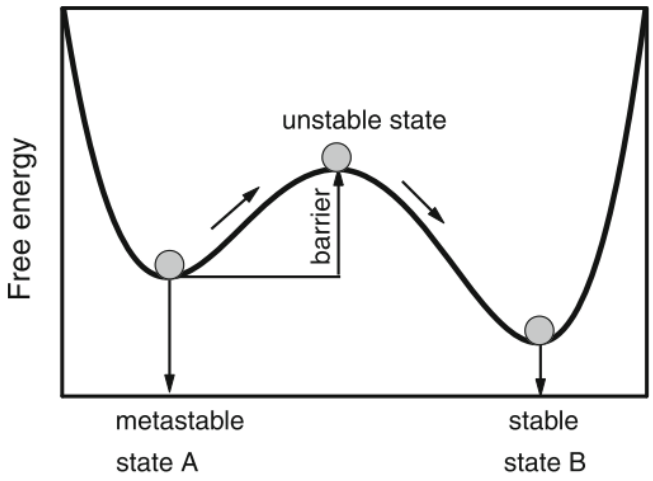

Figure 1.6 Schematics of the free energy curve as a function of the reaction coordinate. Local minimum that corresponds to a metastable state is separated by the global minimum (stable state) with an energy barrier [17].

Overcoming the energy barrier between these two states by the help of thermal fluctuations, the system will undergo a phase transformation. In classical theory of nucleation this energy barrier is directly associated with the phenomenon of *nucleus* formation process which is energetically described by two competitive factors: the energy surplus that is gained by the emerging stable phase with lowest free energy, and the necessary energy to form the interface between the metastable parent and the stable nucleus. Assuming a perfectly spherical nucleus, these competing factors can be calculated using the terms given in the right side of the equation 1.3 in respective order, and their contribution to the net free energy with respect to radius of the nuclei is given in Figure 1.7.

$$\Delta G = \frac{4}{3}\pi r^3 \Delta G_v + 4\pi r^2 \gamma \qquad (1.3)$$

Where γ is the surface free energy, ΔG_v is the free energy of the bulk phase and r is the radius of the nucleus.

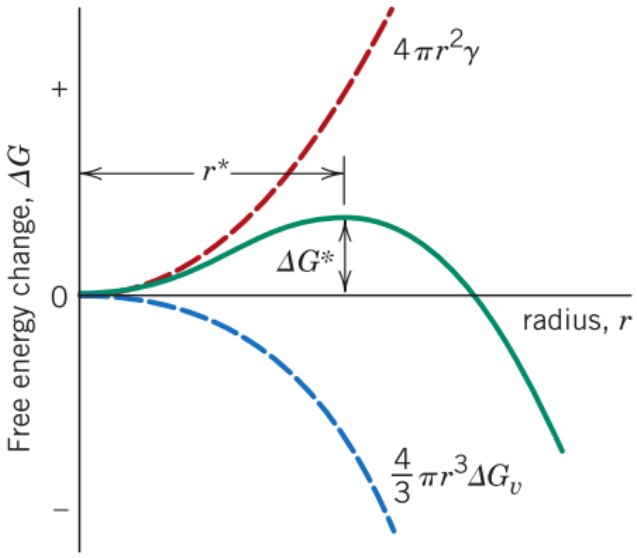

Figure 1.7 Contributions for bulk free energy (blue) and interfacial free energy (red) to the net free energy change (green) associating with the formation of a spherical nucleus of the stable phase [23].

The initial formation and growth process of the nucleus is thermodynamically unfavorable and requires thermodynamic fluctuations in the system. However, as the nucleus grows, cubic bulk free energy term surpasses the quadratic interfacial free energy term. After a critical point, where the differential of the free energy with respect to radius is zero (equation 1.4), growth of the nucleus becomes thermodynamically favorable (spontaneous). The corresponding critical nucleus size, r^*, and the nucleation barrier, ΔG^*, is derived from equation 1.4 as in equations 1.5 and 1.6.

$$d(\Delta G)/dr = 4\pi\Delta G_v r^2 + 8\pi\gamma r = 0 \qquad (1.4)$$

$$r^* = -2\gamma/\Delta G_v \qquad (1.5)$$

$$\Delta G^* = {16\pi\gamma^3}\Big/{3\Delta G_v{}^2} \qquad (1.6)$$

1.4 Experimental Characterization Techniques

In this section, experimental characterization techniques that are widely used in order to probe the local structure and chemistry of disordered systems was summarized.

1.4.1 X-ray and Neutron Diffraction

X-ray diffraction (XRD) is the most prominently used characterization technique in order to determine atomic structure of materials. In crystalline materials, the peaks that occur in intensity vs. diffraction angle ($I\ vs.\ 2\theta$) plot is related with the wavelength of the electromagnetic radiation and spacing between crystallographic planes as stated in Bragg's Law [24]:

$$2d \sin\theta = n\lambda \qquad (1.5)$$

where d is the interplanar spacing, θ is the diffraction angle, and λ is the wavelength of the radiation. In amorphous materials, there are no sharp peaks in the diffraction pattern; since there are no crystallographic patterns possessing translational symmetry. However, the diffraction pattern of amorphous materials have some characteristics that would reveal the local structural information. Instead of sharp peaks that correspond to crystallographic planes, there is a set of broad peaks that correspond to short-range order (SRO) which is the ordering of the atoms in the first-neighbor shell. In some metallic glasses such as Al-RE glasses and covalent silicate glasses, a pre-peak appears in the diffraction pattern. This pre-peak is usually associated with a higher range of ordering; namely, medium-range order (MRO) [25], [26].

In Figure 1.8, the difference between crystalline and amorphous diffraction patterns on the same $Ag_{40}Cu_{60}$ alloy, and intermediate stages during the transformation from amorphous to crystalline during vitrification. While the XRD pattern of the amorphous phase consists of few broad peaks, sharp diffraction peaks corresponding to crystallographic planes starts to form as the amount of crystalline phases increase.

Neutron diffraction has the same principles of X-ray diffraction; however, they differ in terms of atomic scattering factors which is the scattering intensity of elements as

response to incoming photons or neutrons. In X-ray diffraction, electrons of atoms interact with photons; on the contrary, neutrons are scattered from atomic nuclei in neutron diffraction [24].

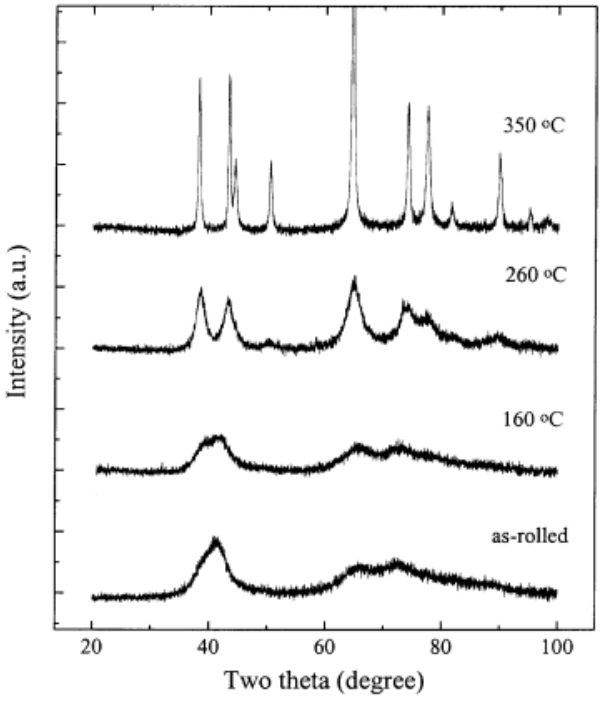

Figure 1.8 Evolution of XRD pattern of $Ag_{40}Cu_{60}$ during transition from amorphous to crystalline structure while heating [27].

1.4.2 Extended X-ray Absorption Fine Structure

Extended X-ray absorption fine structure technique (EXAFS) consists of the measurement of element specific X-ray absorption coefficients of a material by the use of synchrotron radiation. The method is useful to identify the chemistry of surrounding atoms and average coordination number of atoms of an element. Furthermore, pair distribution functions can be extracted from EXAFS via Fourier Transform as in the case of diffraction experiments [2].

1.4.3 Atom Probe Tomography

Atom probe tomography [28] (APT) provides a 3D reconstruction of a material by separating individual ions from the sample using pulsed laser beam, and projecting these ions on a mass spectrometer in order to determine both the location and elemental type of the atoms. The spatial resolution varies between depth and lateral axes, and the resolution is higher in the depth direction. However, the resolution is directly related to crystallography of the specimen and local topology of the specimen surface [29].

The spatial resolution of APT is insufficient to make structural comparisons with computer simulations. However, the chemical information is comparable with computational methods; since, chemical heterogeneities within the range of few nanometers can be revelaed by the use of APT, as in the example of Figure 1.9.

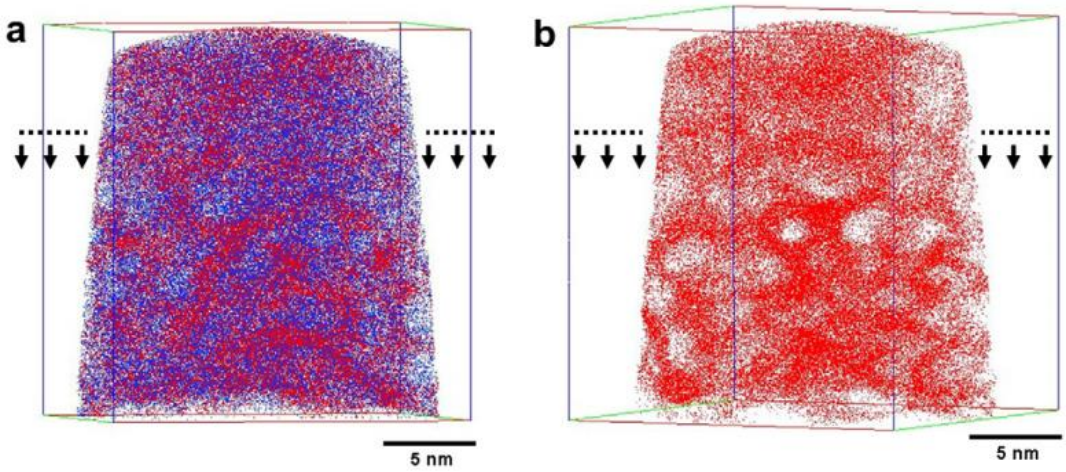

Figure 1.9 Resulting 3D reconstruction of AlSm alloy from an atom probe tomography experiment: (a) Al (blue) and Sm (red) atoms and, (b) Sm atoms only [30].

1.4.4 Transmission Electron Microscopy

Transmission electron microscopy (TEM) can provide structural information from thin specimens of disordered materials having thickness lower than 100 nm by both direct imaging, and electron diffraction. Direct imaging results in 2D projection of 3D samples. On the other hand, 2D electron diffraction patterns can be used for the

extraction of pair distribution functions as in X-ray and neutron diffraction experiments.

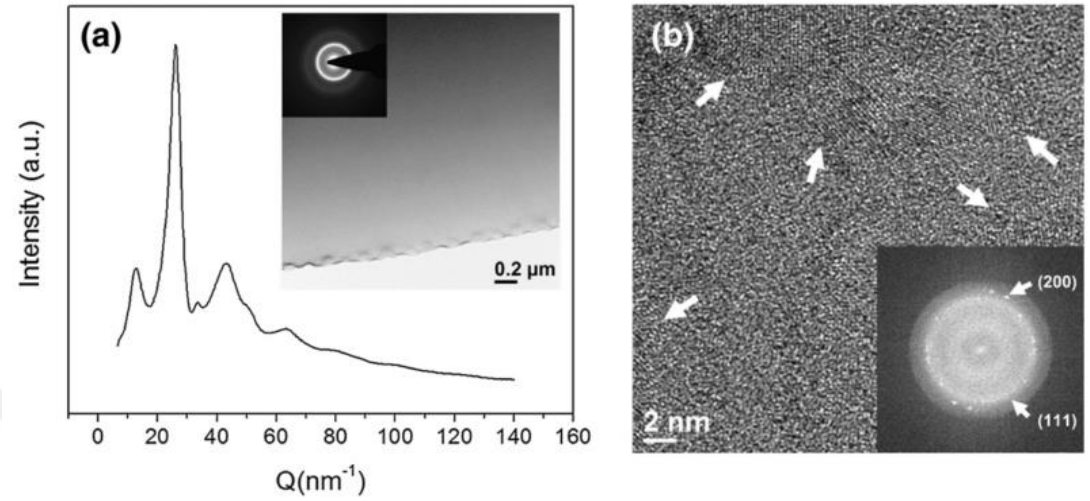

Figure 1.10 (a) High energy XRD (Inset: bright field TEM image and selected area electron diffraction pattern) and (b) high resolution TEM image of Al90Sm10 glass (Inset: FFT of HRTEM image) [31].

As seen in the Figure 1.10, nanocrystalline structures embedded in the amorphous medium can be detected by the use of direct imaging of TEM, and their crystallographic orientations can also be determined from the diffraction pattern.

1.4.5 Fluctuation Electron Microscopy

Fluctuation electron microscopy is a method that enables to detect the structural variations within disordered materials by analyzing a series of diffraction patterns that are obtained from various regions from the sample. As illustrated in Figure 1.11 [32], several diffraction patterns are collected, while the focused probe is scanned over the specimen. Then, the mean and variance of diffraction patterns over all diffraction patterns are calculated.

The peaks in the normalized variance, $V(k)$, versus reciprocal space vector, k, is indicates the presence of medium range order (MRO). Normalized variance is calculated as:

$$V(k,R) = \frac{\langle I^2(k,R,r)\rangle}{\langle I(k,R,r)\rangle^2} - 1 \qquad (1.6)$$

where R is the probe diameter and r is the probe position.

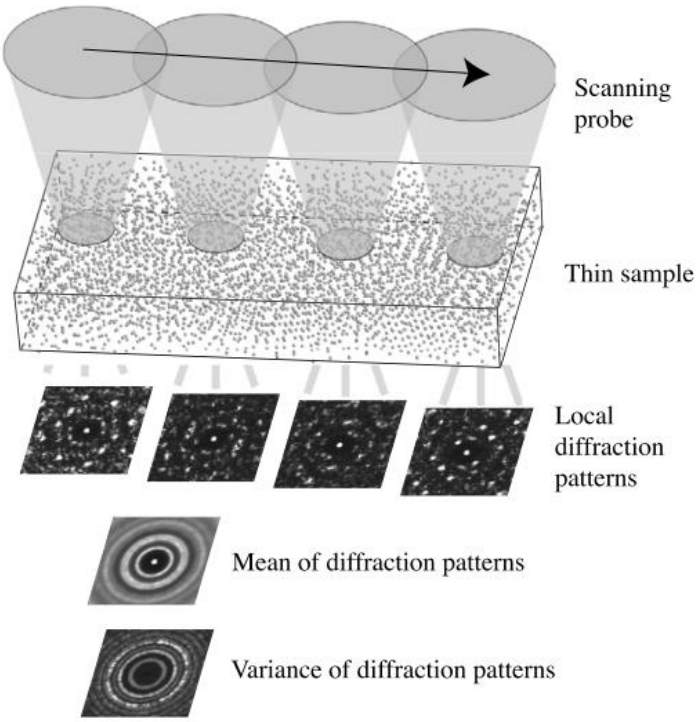

Figure 1.11 The summary of fluctuation electron microscopy methodology [32].

1.5 Thesis Organization

While experimental methods are limited in accessing information at lower time scales, computational methods have an upper limit due to limited computational times. However, many interesting physical phenomena including nucleation resides in the gap between these two classes of methods (Fig. 1.12).

The aim of this thesis is to study topological and chemical structure liquid and of aluminum-based marginal glass forming alloy systems in atomistic scales by the use of computational methods in order to explain the formation of extremely high density of nanocrystals during vitrification. The first chapter covers the general properties of metallic glasses, and thermodynamic and kinetic aspects of glass transition and nucleation, and summarizes experimental characterization techniques that are used to study the structure of metallic glasses. The second chapter focuses on the details of atomistic simulation techniques and computational analyses that are frequently used throughout the study. Third chapter consists of interatomic potential development for $Al_{91}Tb_9$ system using X-ray diffraction data and further investigation on the local structural evolution of $Al_{91}Tb_9$ system from liquid to glass form by the use of Monte Carlo and Reverse Monte Carlo techniques.

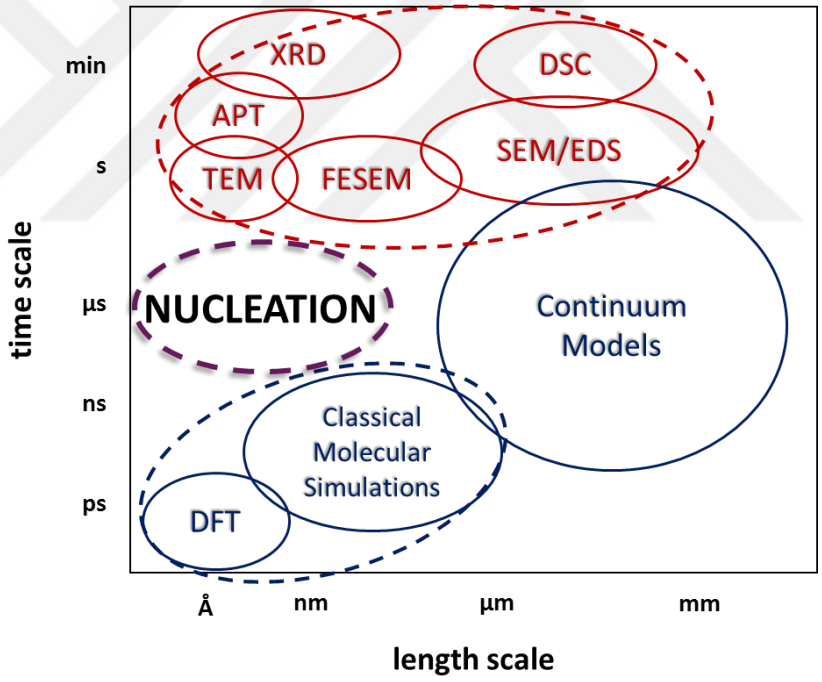

Figure 1.12 Physical limits of experimental methods in terms of space and time. The nucleation phenomena occur in such length and time scales that cannot be directly observed by these two classes of methods.

CHAPTER 2

ATOMISTIC MODELING AND COMPUTATIONAL ANALYSES ON STRUCTURE OF LIQUIDS AND GLASSES

2.1 Atomistic Modelling Techniques

Two most common techniques used in atomistic simulation of liquids and glasses are: Monte Carlo (MC) and molecular dynamics (MD) methods [33], [34]. Monte Carlo simulations are mostly suitable for reaching the lowest energy state of the system, i.e. thermodynamic equilibrium. However, it is not equally favorable for simulating dynamic phenomena. This is mainly because MC simulation is governed by random steps that are independent of time in order to reach energy minima as quickly as possible. Classical MD simulations are also commonly used to reach thermodynamic equilibrium; however, its main advantage is its ability to simulate the dynamic behavior of the system in given amount of time at a nonequilibrium state, since it is governed by Newtonian equations of motion [35].

The other most important aspect of atomistic simulations is to introduce suitable interatomic potentials that are mainly responsible for the thermodynamic and kinetic behavior of the system during simulation. There are a lot of models and methods for determining and applying interatomic potentials. For each system only a finite subset of these models are useful, and there are some advantages each of them would serve and drawbacks that should be considered while choosing the suitable one for the specific simulation.

The theory of atomistic modeling is an endless topic; and, the practice of modeling is also another matter of art. Therefore, it is necessary to refer common and important techniques in computational materials science. In this subchapter, brief theory and

implementation of molecular dynamics and Monte Carlo methods will be described; then interatomic potentials that are frequently used in liquid and glass modelling, particularly in metallic systems, will be cited. Finally, practical computational techniques that are commonly used in atomistic modelling will be examined.

2.1.1 Molecular Dynamics

In a classical molecular dynamics simulation, a system of N particles at a given thermodynamic conditions (constant volume and temperature; NVT ensemble, or constant pressure and temperature; NPT ensemble) is initiated with a specific particle configurations. Then, the behavior of the system is modelled by solving Newtonian equations of motion for each particle simultaneously as described below until the total energy converges to a point that is thermodynamic equilibrium in order to make further measurements [36].

Initialization of the system is typically made by forming a lattice structure such as fcc or bcc even in the simulation of liquids not because, the atomistic configuration at thermodynamic equilibrium is expected to be close to such crystal structure, but rather due to the fact that random initiation of atoms in molecular dynamics would result in atomic pairs that are unphysically close to each other and exert repulsive forces having astronomical magnitudes and push the atoms out of the boundaries of the simulation box. Determining a cut of distance while initiating atom positions randomly may fix this problem however, it would result in exhaustion of possible positions that an atom can fit in an initial volume.

After initial positions are determined, initial velocities of atoms are assigned so that the average kinetic energy of particles should be consistent with the initial desired temperature; because, temperature average velocity of atoms is dependent to each other in single component systems as:

$$E_k = \frac{1}{2}mv^2 = \frac{3}{2}kT \qquad (2.1)$$

where k is the Boltzmann constant, m is mass and v is the average velocity and $E_k$is the average kinetic energy of an atom.

Unlike non-spherical particle systems in which both translational and rotational motion should be included, the behavior of spherical particles can be modelled considering only translational motion, and treatment of rotational motion is inessential. Therefore, in metallic systems, atoms can luckily be treated as spherical particles which reduces computational complexity and saves effort and time.

As described before, in classical molecular dynamics, motion of particles are simulated according to the laws of classical mechanics. Newton's well-known equation of motion is:

$$f_i = m_i \frac{d^2 r_i}{dt^2} \qquad (2.2)$$

where force vector, f_i, applied on the i^{th} particle divided by mass, m_i, of the particle results in the second derivative of the position vector of the particle with respect to time. Therefore, the motion of the particle can analytically be determined in any time according to the equation above.

In a system of N particles, it is impractical solve a set of N differential equations for each time step analytically. Therefore, the above expression should be somehow approximated by a transformation into an algebraic equation. The second derivative of the position vector can be evaluated by "central difference approximation" as:

$$\frac{d^2 r_i(t)}{dt^2} = \frac{r_i(t+h) - 2r_i(t) + r_i(t-h)}{h^2} \qquad (2.3)$$

by the use of Taylor series expansion of $r_i(t+h)$ and $r_i(t-h)$ terms. Then, Newton's equation of motion can be rewritten as:

$$r_i(t+h) = 2r_i(t) - r_i(t-h) + \frac{h^2}{m_i} f_i(t) \qquad (2.4)$$

Similarly, by using Taylor series expansion velocity of a particle at a given time can be approximated as:

$$v_i(t) = \frac{dr_i(t)}{dt} = \frac{r_i(t+h) - r_i(t-h)}{2h} \qquad (2.5)$$

$$r_i(t+h) = r_i(t) - hv_i(t) + \frac{h^2}{2m_i} f_i(t) \qquad (2.6)$$

Resulting scheme is called "Verlet method" [37]. Therefore, we obtain a basic procedure for conducting the molecular dynamics simulation step by step:

1. Specify the initial position and velocity of all particles.
2. Calculate the forces by the use of interatomic potentials.
3. Evaluate the positions of particles at next timestep from equation (2.6).
4. Evaluate the velocities of particles at next timestep from equation (2.5).
5. Repeat the steps from step 2.

2.1.2 Monte Carlo

Monte Carlo is a stochastic method that was developed in order to solve a broad range of problems in mathematics and physics numerically by iteratively producing randomized numbers. Its applications may be divided into three main categories: (1) numerical integration, (2) generating a sample dataset from a given probability distribution, and (3) optimization. As the implementation specifics vary for each possible application, the principle of generating an input consisting of a set of random numbers remains constant.

In order to gain further intuition, the most simple example of Monte Carlo method is to be considered which is the approximation of the well-known mathematical constant, π, by numerical integration of a circle [38]. Consider a quarter unit circle having an area of π/4 that is contained by a unit square having an area of 1 as shown in Figure 2.1. The area of this quarter circle relative to its container square can be calculated by the use of Monte Carlo method of integration.

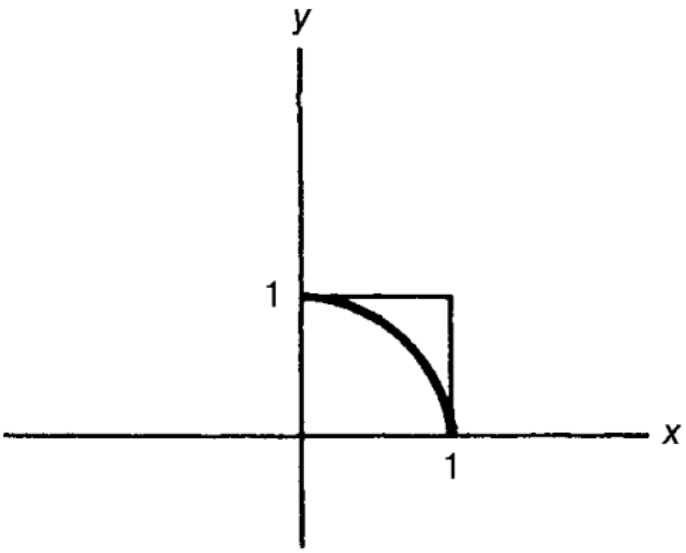

Figure 2.1 A quarter of unit circle contained by a unit square [38].

If we choose a random point within the domain $0 \leq x \leq 1$, and $0 \leq y \leq 1$, the probability that the point resides in the quarter circle is the area of quarter circle divided by the area of square, which is π/4. As points are introduced, it is also possible to check whether the point is within the circle or not by simply calculating its distance from the origin. Therefore, when we have several points within the specified domain (inside the square), π can be approximated by the following formula:

$$\pi = 4\frac{\#\ of\ points\ inside\ the\ circle}{Total\ \#\ of\ points} \qquad (2.7)$$

As the sample set is increased, the result will be much more statistically significant and converge to the analytical value of π. It is stated that after generating 1,000,000 points, it is very likely (95% chance) that the number of points that will reside within the boundaries of the circle will be between 784,600 and 786,200 [38]; therefore the estimated value of π will be between 3.1384 and 3.1448, compared with the true value of 3.14159.

Optimization problems are classically solved by differential calculus. A typical optimization problem is traditionally represented by a function of several parameters

that is to be minimized, often referred as a cost function. In most practical cases, analytical differentiation of the function in order to reach the minimum, may not be feasible. In these cases, numerical method such as Newton's method (also known as Newton-Raphson method) or gradient descent method is used [39], [40]. These methods are based on a procedure of taking steps in the opposite direction to the gradient of the function of the current point, iteratively; therefore, guaranteeing to decrease the value of the cost function at each step until reaching to a minimum. However, these methods are failed in the case of multiple local minima, since the algorithms tend to be terminated at a local minima that is nearest to initial point, which may yield to a result that is far from the optimum solution, i.e. the global minimum. In these cases, stochastic optimization methods are used in order to overcome the hills on the cost function surface that separate these local minima by a degree of randomization in the changes in the function parameters.

Molecular simulations are optimization problems in their essence. For example, a typical molecular simulation consist of fixed number of atoms, N, interactions among each other are governed by interatomic potential functions. Interatomic potential is typically a function of energy with respect to relative spatial positions of the particles. At a constant volume V and temperature T (as in the case of canonical ensemble), a molecular simulation aims to minimize the energy in order to identify the behavior of the system at its thermodynamic equilibrium. The total energy of the system can be calculated by the use of interatomic potentials at a given time. In this manner, the molecular simulation can be considered a problem of optimization having a cost function of total energy having 3N parameters involving the positions of N particles in 3-dimensional space. There are infinitely many possible particle configurations, and there is no analytical way to find a minimum for this kind of problem. A Monte Carlo simulation framework provides a simple and elegant approach. If we change the position of particles randomly within a specified domain, we are able to recalculate the energy of the system and see whether the system approaches to a minimum or not. If it is, the positional change is accepted, and continue with another random change in positions, else we simply reject the change, and retry.

Using this approach the system will converge to a minimum; however, in this case, Monte Carlo is not the most feasible solution among the abovementioned methods. As compared with gradient descent in which system is guaranteed to gravitate towards a minimum at each step, Monte Carlo consist of many unnecessary steps that would increase the energy, and therefore, will be rejected. The reason why Monte Carlo is superior to gradient descent or other alternatives is the fact that it can be extended so that it will not stuck into a local minimum but it can lead the system to lower minima by selectively accepting steps that increases the total energy by the use of another level of randomization. This approach is called Metropolis algorithm [41].

In the Metropolis algorithm, following workflow was proposed:

1. Select a random particle from the system, and calculate its energy $U(r)$,
2. Change the particle position with a random displacement within a specified domain as: $r_{new} = r_{old} + \Delta r$,
3. Calculate the energy of the particle in its new position $U(r')$,
4. If $U(r') - U(r) \leq 0$, then accept the move; otherwise, accept the move by the probability If $\exp(U(r') - U(r)/kT)$
5. Repeat the steps until system energy converges to an equilibrium.

Notice the probability of accepting the move in the case of energy increase is an Arrhenius-type equation which provides temperature dependence of reaction rates by considering the Maxwell-Boltzmann distribution. In other words, the term, $\exp(U(r') - U(r)/kT)$, provides the probability that whether a particle has necessary kinetic energy in order to climb up a potential energy barrier, $U(r') - U(r)$, or not. This approach, therefore, provides a physical basis for modelling thermal averages of a system by passing over local minima.

2.1.2.1 Reverse Monte Carlo

While the primary purpose of conventional Monte Carlo simulation that is governed by interatomic potentials is to minimize the total energy of the system, the reverse Monte Carlo (RMC) method aims to produce a 3-dimensional atomistic model that is

consistent with experimental data. The method is particularly useful to model non-crystalline structures in which the pair distribution functions (PDF) are correlated with diffraction experiments via Fourier transform after making some corrections. RMC was initially proposed by McGreevy et. al. [42] by the use of experimentally measured structure factor, $S(Q)$, of liquid argon. The procedure is summarized as:

1. Initially, N number of atoms is placed into a cubic simulation box having an edge length of L. The configuration may be generated randomly, or by using a lattice structure, or by obtaining an atomic configuration from a conventional molecular simulation.
2. Radial distribution function of the simulation box, $g'_S(r)$, is calculated, where periodic boundary conditions have been applied.
3. Configuration is changed by selecting and displacing an atom randomly, and $g_S(r)$, is calculated again.
4. Experimentally obtained radial distribution function, $g_E(r)$, and that of the simulated model were compared by the use of chi-squared test:

$$\chi^2 = \sum_{i=1}^{n_r} \left(g_E(r_i) - g_S(r_i) \right)^2 / \sigma_E^2(r_i) \qquad (2.8)$$

$$\chi'^2 = \sum_{i=1}^{n_r} \left(g_E(r_i) - g'_S(r_i) \right)^2 / \sigma_E^2(r_i) \qquad (2.9)$$

   where n_r is the number of discrete points constituting the radial distribution functions, and σ_E is the experimental error.
5. If $\chi \leq \chi'$, then accept the displacement; otherwise, accept the displacement by the probability that follows a Gaussian distribution with a standard deviation σ.
6. Steps 2-5 are repeated until χ^2 decreases and converges to an equilibrium value.

RMC method also allows the improvement of the model by introducing additional constraints and experimental data such as the addition of coordination number constraint in order to model tetrahedral local structure of amorphous silicon [43], addition of bond angular constraints in order to model molecular structures [44], introducing the extended X-ray absorption fine structure (EXAFS) data which

provides better insight on local structure as compared to X-ray diffraction [45]. Additionally, in binary systems in which partial pair distribution functions cannot be uniquely determined by a single diffraction technique. Combined use of multiple diffraction techniques [46]–[48] such as X-ray diffraction, electron diffraction and neutron diffraction will yield three different structure factors; since, atomic scattering factors that is unique to an element differ for each diffraction technique. Therefore, obtaining three different structure factors results in a determined linear system while calculating all three partial pair distribution functions in binary systems.

Hybrid Reverse Monte Carlo (HRMC) is a method combining reverse Monte Carlo and conventional Monte Carlo in a sense by introducing of energy constraint to RMC system while the system energy is calculated by interatomic potentials. The method is being used particularly for investigating the structure of carbon-based materials such as activated [49], porous [50], saccharose-based [51] and amorphous carbon solids [52], [53].

2.1.2.2 Inverse Monte Carlo

In statistical mechanics, the statistical analysis is ordinarily made in position space, while the particle interactions are given. On the other hand, the inverse problem of statistical mechanics is posed that given a spatial distribution of atoms, the interatomic potentials that govern the energetics of the system (i.e. the Hamiltonian of the system) is to be determined [54]. Microscopic structure of a system can be modelled by using RMC as described above, or pair distribution functions was thought to efficiently used represent the configuration of the system in order to solve the inverse problem; because, it has been shown that if a system is able to be described by additive pairwise potentials, there is a unique relationship between the pair distribution function and interatomic potentials [55].

Almarza and Lomba [56] have been described a procedure to evaluate pair potentials that are compatible with experimentally obtained pair correlation functions by the use of Monte Carlo framework. The resulting method has been named as inverse Monte

Carlo technique. Summarily during a classical Monte Carlo simulation of a system in which experimental pair distribution functions were previously obtained, Initially assigned pair potentials are progressively altered according to the difference between simulated and experimental pair potentials until the difference is minimized. The algorithm is as:

1. Assign an initial particle configuration (for example, an fcc lattice structure) and estimate the initial interatomic potential as:

$$\beta v(r_i) = -\ln\big(\mathrm{g}(r_i)\big) \tag{2.10}$$

   where $\beta = 1/kT$.
2. Start the simulation at the first stage ($l = 1$).
3. At each stage l and after each cycle of N displacements compute the radial distribution function of the stage, $\mathrm{g}_l(r)$, averaged over several configurations and modify $\beta v(r)$ such that,

$$\beta v^{new}(r_i) = \beta v^{old}(r_i) + \lambda_l \frac{\mathrm{g}_l(r_i) - \mathrm{g}_{target}(r_i)}{\Delta \mathrm{g}_l(r_i)} \langle \Delta \mathrm{g}_l(r_i) \rangle \tag{2.11}$$

$$\langle \Delta \mathrm{g}_l(r_i) \rangle = \frac{1}{m} \sum_{i=0}^{m-1} \Delta \mathrm{g}_l(r_i) \tag{2.12}$$

4. After each cycle, convergence criterion is checked:

$$\langle \Delta \mathrm{g}_l(r_i) \rangle = \frac{1}{m} \sum_{i=0}^{m-1} \left(\frac{\mathrm{g}_l(r_i) - \mathrm{g}_{target}(r_i)}{\Delta \mathrm{g}_l(r_i)} \right)^2 \leq \eta \tag{2.13}$$

   where $\eta \cong 1$
5. If convergence condition is fulfilled, the next stage $l + 1$ is initiated in which the modifying parameter λ is decreased

$$\lambda_l = \alpha \lambda_l = \alpha^{l-1} \lambda_1 \tag{2.14}$$

   where $0 < \alpha < 1$

At first stages the pair potential gains its main features; however, numerical noise is significant due to relatively large values of modifying parameter λ, then the potential function is refined and gets smoother at the later stages. At final stages, the change in the pair potential function becomes negligible and Monte Carlo simulation reaches to the structural equilibrium where the pair distribution function in the simulation

converges to the target pair distribution function. Therefore, the resulting pair potential is able to reproduce structural identity of the system as observed from diffraction experiments.

2.1.3 Interatomic Potentials

Interatomic potentials are critical in simulating physical behavior of the system by assigning potential energy to atoms according to their interactions with surrounding atoms. In molecular dynamics, the first differential of the interatomic potentials results in interatomic forces providing the information on the acceleration vector of an atom at a given time; on the other hand, in Monte Carlo, it is evaluated that whether a random displacement is feasible at these potential energy levels in terms of statistical mechanical concepts. The classical interatomic potentials may be divided into two main categories: pair potentials, and many-body potentials.

The simplest interatomic pair potential is the model of hard spheres that is mathematically described as:

$$V(r) = \begin{cases} \infty \,; r < \sigma \\ 0 \,; r \geq \sigma \end{cases} \qquad (2.15)$$

where r is the distance between two particles. If particles are separated with a distance lower than σ the potential energy is infinitely large, however if the distance is higher than σ the potential energy is zero. Therefore, it is impossible or illegal that two particles become closer than σ, as in the case of hard spherical particles having radius of $\sigma/2$. Initial use of this potential was the case of "hard disks" in which 2-dimensional hypothetical systems were modelled as in the case of Metropolis et. al. [41]. In the case of hard spheres there is also no physical motivation in terms of representing a real system according to the interactions between particles; however, the model still gives intuition to the behavior of fluids and solids [57]–[59] and topological theories of glass-forming metallic alloys such as Miracle model [60]–[62].

Another widely used interatomic pair potential is the Lennard-Jones potential [63] which has the mathematical form:

$$V(r) = \varepsilon \left[\left(\frac{r_m}{r} \right)^{12} - 2 \left(\frac{r_m}{r} \right)^{6} \right] \qquad (2.16)$$

where r is the distance between two particles, ε is the potential minimum, and r_m is the distance at which the potential reaches its minimum. At short distances the first term becomes highly dominant due to Pauli exclusion principle which states that two electrons cannot occupy the same quantum state resulting a strong repulsive electron-electron interactions with increasing magnitude as two atoms get closer. However, at longer distances second terms become dominant and atoms attract each other due to van der Waals interactions. There are some other variants such as Buckingham potential [64] in which the repulsion energy due to Pauli exclusion principle is described by an exponential term while van der Waals attraction remains practically the same. Lennard-Jones model accurately describes the interactions among noble gas atoms such as helium and argon, and it is also used to investigate the behavior of hypothetical condensed systems as there are a lot of studies on Lennard-Jones solids, fluids, glasses and interfaces on systems having both single and multiple components [65]–[68]; however there are considerable limitations when modelling real condensed systems such as elastic properties, and force constants; that cannot be accurately represented by solely two parameters.

Morse potential [69], which has the following mathematical form, provides an improvement by introducing an additional degree of freedom:

$$V(r) = D_e[\exp(-2a(r - r^e) - 2\exp(-a(r - r^e)] \qquad (2.17)$$

where r is the distance between two particles, D_e is the equilibrium bond energy, r^e is the equilibrium bond distance, and a is the potential well width. The additional potential well width term that is obtained by solving the Schrödinger equation representing the motion of the atoms in a diatomic molecule [70] provides a better approximation for the vibrational structure of atomic pairs. Therefore, Morse potential is a lot more suitable in modelling physical properties such as energy of vaporization, compressibility and the lattice constant along with the elastic constants in face-

centered and body-centered cubic metals; therefore, Morse potential is considered as the most basic interatomic pair potential in order to model cubic metals [71].

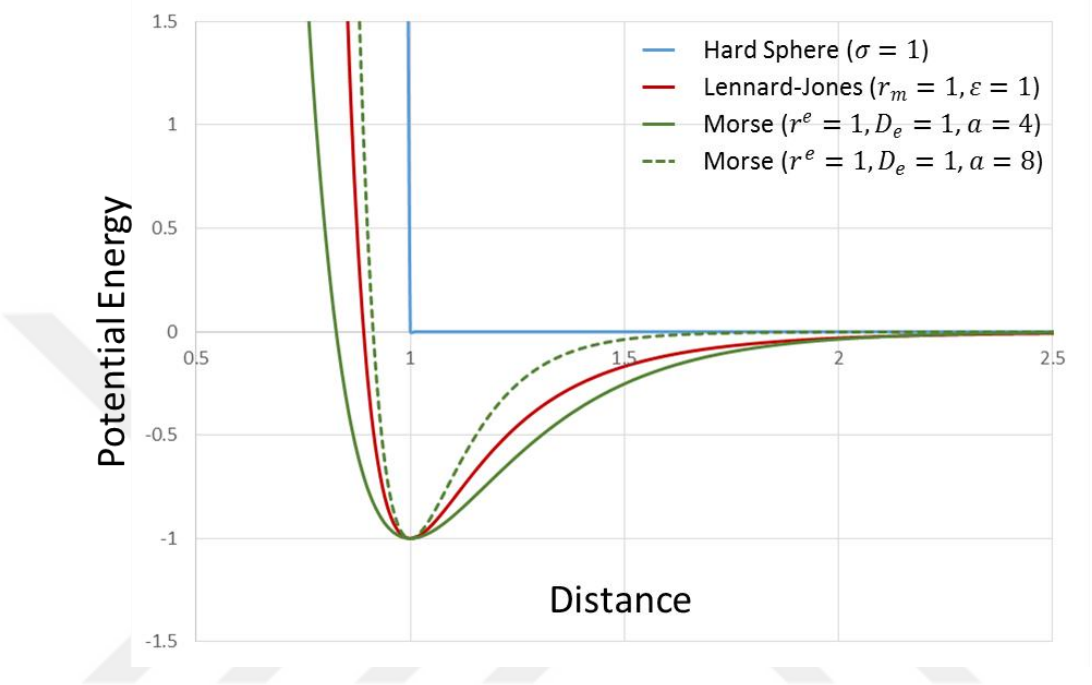

Figure 2.2 Comparison of the most common interatomic potentials: hard sphere (blue), Lennard-Jones (red), Morse with a broader potential well (green), and Morse with a narrower potential well (green, dashed).

In Figure 2.2, all three interatomic pair potentials are illustrated with parameters having arbitrary units as an example. All three potentials are given the same bond length of 1. As there is no potential well in hard sphere model, well depth of Lennard-Jones and Morse potentials are also assigned the same as 1. Finally, while potential well width of Lennard-Jones model is constant, it can be adjusted in Morse potential which gives more control on modelling several physical phenomena such as thermal expansion, compressibility and vibrational properties.

Coulombic interactions can also be introduced to these potentials in order to model pairwise interactions between ionic species by adding the term for electrostatic potential energy:

$$V(r) = \frac{q_1 q_2}{4\pi\varepsilon_0 r} \qquad (2.18)$$

where r is the distance between two particles, $\varepsilon_0$is the vacuum permittivity (i.e. electric constant)

Interatomic pair potentials, potential energy is dependent only on the pair distance. However, unlike the presence of independent pair interactions, in real systems, bonding characteristics between two atoms are fairly affected by their environment i.e. surrounding atoms. For example, as packing density increases, especially in condensed matters, the bond strength will generally decrease as a result of repulsive forces among electrons due to Pauli principle. Therefore, interatomic potentials that would describe the system more accurately should adapt to local chemistry. Additionally, directional bonding in which angular relations are highly important bonding cannot be represented due to spherical symmetricity of pair potential functions.

Stilinger-Weber potential [72] is particularly important because it provides a simple and accurate description of the many-body interactions by including three-body interaction terms into pairwise interactions in order to model the directional nature of the covalent bonding in silicon crystals having following form:

$$V = \sum_{i,j} v_2(r_{ij}) + \sum_{i,j,k} v_3(r_i, r_j, r_k) \qquad (2.19)$$

where three-body term describes the change in the potential energy with the change in the bond angle. Many variants of Stilinger-Weber have been proposed to model elemental and compound semiconductors [73]–[75]; however these potentials remain primitive in order to model subtle many-body interactions that result in significant changes in observable properties in materials having directionless bonding.

Embedded atom model [76] is a many-body interatomic potential framework that is widely used to model particularly metallic systems at the present time. It takes advantage of highly delocalized electrons in metallic bonding, and it introduces the local environmental dependence of potential energy of an atom that was discussed above by including electron charge density of space. While each atom affects the charge density of surrounding space according to its elemental type, the presence of any atom at a point in space, having a charge density that is dictated by surrounding atoms, affects its potential energy that is described by its element-specific embedding function. Thus, the total potential energy of an atom i takes the form:

$$E_i = F\left(\sum_{i \neq j} \rho(r_{ij})\right) + \frac{1}{2}\sum_{i \neq j} \phi(r_{ij}) \qquad (2.20)$$

where r_{ij} is the distance between atoms i and j. The second term is the potential energy related with pairwise interactions, where $\phi(r_{ij})$ is the pairwise potential function. F is the so-called embedding function that is the amount of energy required to place atom i to the point having an electron density of $\sum_{i \neq j} \rho(r_{ij})$ that is caused by surrounding atoms.

By the rapid development of EAM potentials for several metallic systems, it became possible to conduct simulations on these systems for investigating various physical properties and experimental phenomena [77]–[88]. Calculating the electron charge density and contribution of embedding function to the potential energy makes the use of EAM potentials slower as compared with pairwise potentials by a factor of 2 or 3 in molecular simulations; however, their apparent success in modelling of metallic systems in classical domain makes them very popular. There are EAM potentials of several metallic elements, and binary, ternary, and higher order alloys freely available on open source online repositories [89].

Classical interatomic potentials are based on simplistic models of attractive and repulsive interactions between atoms and some experimental macroscopic observations, and they provide only a rough approximation to actual interactions between atoms which are quantum mechanical in nature. While quantum mechanics

can describe the electron states of small atoms analytically with complete precision, solving Schrödinger equation for all electrons in bigger atoms or several atoms standing next to each other analytically is impossible with the mathematics that is possessed by the humankind today. However, there are several reasonable approximations and numerical methods to solve these problems *ab initio;* from the first principles of quantum mechanics. While there are several methods, density functional theory (DFT) is the most widely used computational quantum mechanical method in order to represent atomic interactions. In fact, these methods provide the only answer that can be considered as real in dimensions where experimental techniques are insufficient. However, switching from classical to *ab initio* methods comes with a serious price. These methods are only feasible at spatial and temporal scales that are smaller of 3-4 orders of magnitude as compared with classical methods.

2.1.4 Tricks of the Trade

Most of the atomistic simulations are conducted with the intention of generating realistic particle behaviors such that these behaviors represent the observable features of real systems at macroscopic scales. Commonly, observable features act on infinitely large dimensions as compared with atomic scales. However, for practical reasons computer simulations should be conducted on limited dimensions due to computational limitations. Moreover, these experimental observations are mostly an average of time scales much longer than computer simulations due to limited time resolutions of experimental methods. Therefore, computer simulations should be designed as efficient as possible to represent the spatial and temporal scales in experiments, while not compromising accuracy.

2.1.4.1 Periodic Boundary Conditions

Dimensions of simulation boxes in atomistic simulations are on the order of nanometers. Therefore, simulation box boundaries should be treated such that the simulation represents the bulk features; otherwise, atoms close to boundaries would

behave as surface atoms, and system energy and other properties would highly be affected from those surface effects.

Periodic boundary condition (PBC) enables to reproduce and explain macroscopic properties accurately by conducting simulations on much smaller systems consisting of 10^2-10^5 atoms [90]. In Figure 2.3, the concept of periodic boundary conditions has been illustrated in a 2-dimensional system. The simulation box is treated as a repeating unit cell where the simulation space is continuous such that the simulation box is surrounded by its own replicas in order to approximate an infinitely large system. When a particle crosses a boundary of the simulation box it reappears near the opposite boundary at the same conditions. Particle interactions are also computed such that particles residing near the opposite boundaries are treated as they are close to each other.

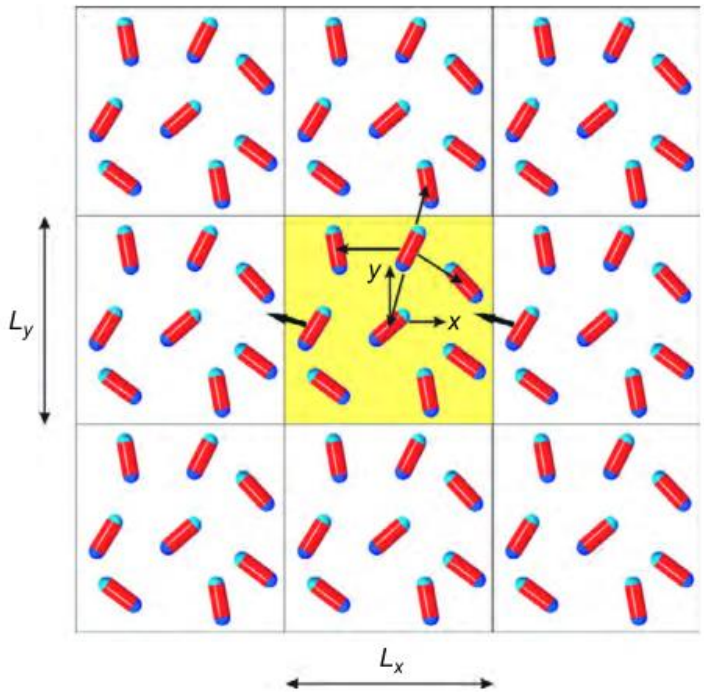

Figure 2.3 Periodic boundary condition [35].

When periodic boundary condition is applied, the simulation box size should be adjusted such that a particle should never interact with its own replica at a neighboring

simulation box, otherwise the simulation would yield unphysical results, especially in molecular systems [91]. Some rare events such as nucleation may also be mistreated as an artifact of periodic boundary conditions. For example, it has been found that rapid crystallization of Leonard-Jones liquid in some cases is related with the presence of periodic boundary conditions and the phenomenon is not a result of the formation of a crystal nucleus exceeding the critical size which was stated in the classical nucleation theory [92]. Another artifact of periodic boundary condition is the pair distribution functions of dense disordered systems is found to be anisotropic [93].

2.1.4.2 Cut-off Distance

The potential energy of a system of two particles separated by a distance of r is calculated as the amount of work required to separate two particles by an infinite distance [94]. The interatomic potential functions that are used in order to model real systems are commonly based on this fact converging to zero at infinity. However, in computer simulations, the range of particle interactions are restricted to finite distances. The distance of ceasing the calculation of interaction energies is known as cut-off distance [35]. After cut-off distance, r_c, particle interactions are considered to be negligible. This treatment saves a considerable computational time: A simulation of N particles without the use of cut-off distances, $N(N-1)/2$ particle interactions needs to be computed at each step resulting in quadratic ($O(n^2)$) computational complexity. On the other hand, while introducing cut-off distances to interatomic potential energies, each particle only interacts with a finite number of neighboring particles within the cut-off distance independent from system size resulting in linear ($O(n)$) computational complexity.

When employing periodic boundary condition, the size of the simulation box should be more than twice of the size of cut-off distance in order to ensure that any particle interacts with only the nearest image of replicated particles and not by themselves. If the system consists of macromolecular particles, this ratio should be much higher in order to prevent the interaction of molecules by themselves.

2.1.4.3 Verlet Neighbor List Method

Whether the separation of any particle pair resides within the range of cut-off distance has to be determined inevitably by computing their distance. However, computing $N(N-1)/2$ pair distance at each step in order to determine whether particles attract to each other is remarkably expensive.

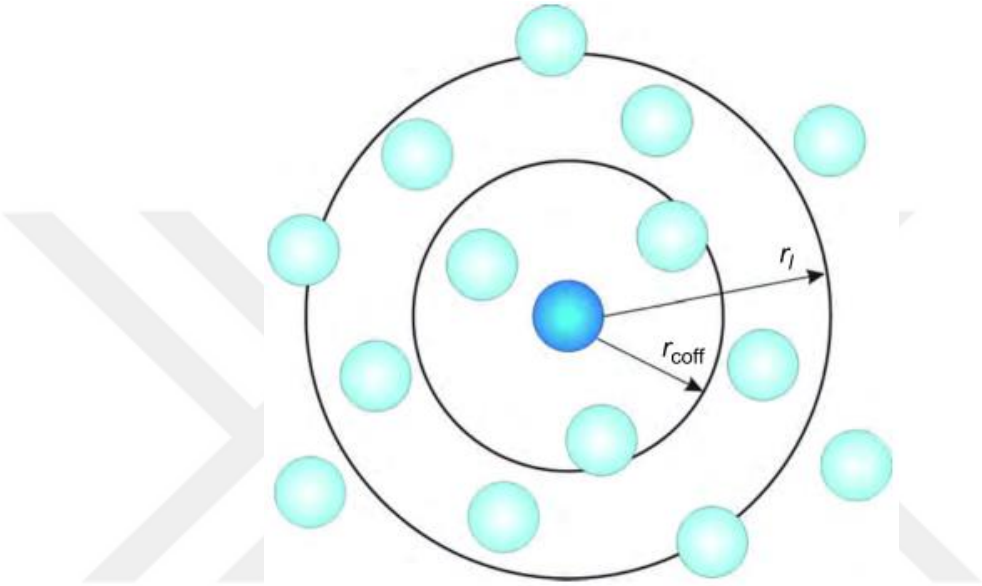

Figure 2.4 Verlet neighbor list method [35].

Verlet neighbor list method proposes an additional distance parameter, r_l, which is larger than the cut-off distance , r_c [95] as illustrated in the Figure 2.4. It is assumed that once the list of neighboring particles for each particle within the distance, r_l, is computed, it is sufficient to compute the distance of particle pairs only residing in the neighbor lists in order to further compute interactions in the subsequent fixed number of simulation steps; because, particles that is not listed in the neighbor list will not get closer to cut-off distance in a given time interval and will not affect the system energy. Therefore, the overall simulation becomes computationally much more feasible without affecting the results by the use of Verlet neighbor lists if the distance, r_l, and number of steps for neighbor lists to be refreshed is carefully specified in order to avoid errors.

2.1.4.4 Cell Index Method

Dividing the simulation cell within sub-cells of equal size which is at least equal to the cut-off distance (r_c) or Verlet neighbor list distance (r_l) provide an additional computational advantage, when determining the neighboring particles [96], [97]. While computing the Euclidean distance of any particle pair consists of several mathematical operations such as computing the square of the coordinate differences for each dimension and the taking the square-root; determining the sub-cell a given particle resides, namely, its cell index, according to its Cartesian coordinates is much simpler.

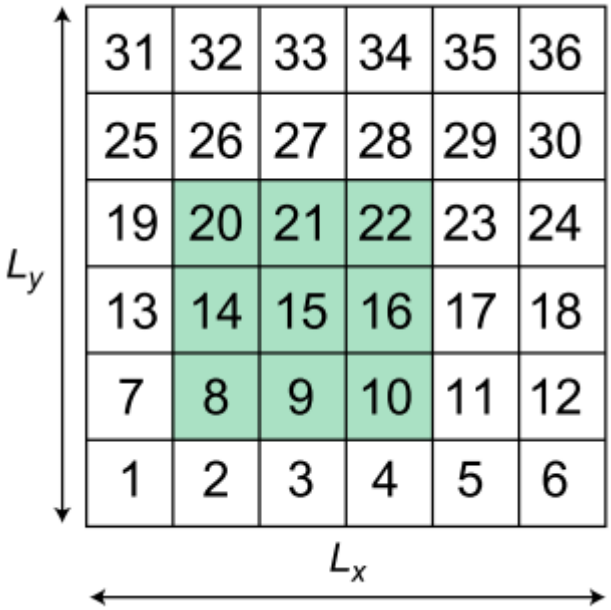

Figure 2.5 Cell index method in order to determine neighboring particle candidates [35].

As shown in Figure 2.5, the indices of neighboring sub-cells for each sub-cell is readily available. While computing particle pair distances in order to compute particle interactions within the range of cut-off distance or construct Verlet neighbor list of a particle, considering only the sub-cell the particle resides and the neighboring sub-cells is sufficient. Therefore, unnecessary computations are avoided.

Verlet neighbor list method and cell-index method can be successfully used together, and their contribution to the computational efficiency become more apparent with increasing system size; however, the method for determining parameters that are used in these methods in order to optimize the computational process is not straightforward and parameters may vary for each system.

2.2 Structural Analyses

Most of the metallic systems of interest are crystalline in the solid form and these systems can be analyzed and interpreted by means of conventional crystallography. The definition of order and deviations from it are well-defined through symmetry rules and crystallographic defects. Mechanisms related with these crystallographic features are highly successful to bridge the gap between atomic structure and macroscopic properties. On the other hand, there is no elegant mathematical model to resolve the ambiguity of the definition and the extent of "order" in non-crystalline systems. However, there are several metrics and methods that have been developed in order to identify the structural patterns and their physical consequences.

2.2.1 Pair distribution function

Pair distribution function (PDF), $g(r)$ is a probability distribution that represents the probability of the presence of an atom that is separated by a distance r, from the central atom that is normalized to the number density of atoms. In systems having more than one component, pair distribution function is specified for each component pair. In this case, the function is called as partial pair distribution function, $g_{\alpha\beta}(r)$, which is defined as:

$$g_{\alpha\beta}(r) = \frac{N}{4\pi r^2 \rho N_\alpha N_\beta} \sum_{i=1}^{N_\alpha} \sum_{j=1}^{N_\beta} \delta(r - r_{ij}) \qquad (2.21)$$

where N is the total number of atoms in the system, ρ is the number density of atoms, and N_α and N_β is the total number of atoms of components α and β, respectively. The dirac delta function which takes the value of zero everywhere except zero is used to count the number of atomic pairs that is separated by the distance of r, where r_{ij} is the

distance between an atomic pair. Since the number density is present in the denominator of the equation, the function converges to unity at longer distances.

Pair distribution function provides limited structural information of the system. The only parameter of the function is the distance r, therefore the function provides the information that is averaged by spherical symmetry. Furthermore, PDF provides only pair correlations, and, three-body angular structures and further many-body structural correlations are not present. Finally, PDF is averaged over every atomic pair, so structural heterogeneities that may be present in the system cannot be directly detected.

On the other hand, pair distribution function is still a powerful structural parameter because it is directly linked to diffraction experiments through the bilateral relationship with the structure factor, $S(Q)$. Partial pair distribution functions can be converted to the partial structure factor $S_{\alpha\beta}(Q)$ by the use of Fourier transform [98],

$$S_{\alpha\beta}(Q) - 1 = \frac{4\pi\rho}{Q}\int_0^\infty r\left[g_{\alpha\beta}(r) - 1\right]\sin(Qr)dr \qquad (2.22)$$

where ρ is the number density of atoms, and Q is the diffraction vector that resides in the reciprocal space having a magnitude of $4\pi\sin\theta/\lambda$ where θ is the angle of diffraction and λ is the wavelength of the monochromatic radiation that is used in the diffraction experiment. Total structure factor $S(Q)$, can be obtained by summing partial structure factors weighted by molar fractions and atomic scattering factors,

$$S(Q) = \sum_\alpha \sum_\beta \frac{c_\alpha c_\beta f_\alpha f_\beta}{(\sum_\alpha c_\alpha f_\alpha)^2} S_{\alpha\beta}(Q) \qquad (2.23)$$

where c_α and c_β are molar fractions of each element, and f_α and f_β are atomic scattering factors which are also functions of Q. In monatomic systems, pair distribution function can be converted to structure factor directly using Equation 2.22.

In Figure 2.6a, pair distribution function of liquid copper at 1500 K is calculated using atomic configurations obtained from molecular dynamics simulation is shown. Structure factor of liquid copper obtained by pair distribution function via Fourier transform is also given in Figure 2.6b. Direct conversion between structure factor and

pair distribution function is consistently used in the development of interatomic potentials that are consistent with experimental observations on liquid and glass structure possible [99]–[102]. Furthermore, using pair distribution functions directly obtained from experimental observations, three-dimensional models of the system are developed using techniques such as reverse Monte Carlo as described before, and further structural analyses such as bond angular distribution, Voronoi analysis etc. are performed which may reveal structural features that may be hidden in diffraction data and give better intuition on short-to-medium range order.

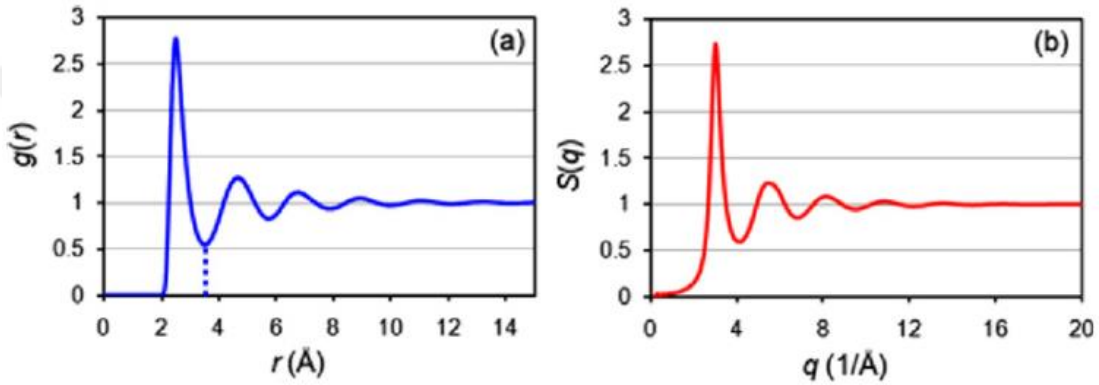

Figure 2.6 (a) Pair distribution function and (b) structure factor of liquid copper at 1500 K, obtained from MD simulation [2].

2.2.2 Voronoi Tessellation Analysis

In Voronoi tessellation analysis of topologically disordered systems, the space is divided into polyhedra by computing plane boundaries between atoms so that the plane equidistant to each atom in the atomic pair. It is necessary to have a position vector (a point in the space) and a normal vector (the vector that is perpendicular to plane surface) to define a plane. Therefore, calculation of the plane boundary between atoms i and j is as follows:

1. Determining the position vector:

$$\vec{r} = 0.5\,\vec{r_i} + 0.5\,\vec{r_j} \tag{2.23}$$

where $\vec{r}$ is the position vector of a point in the boundary plane, and $\vec{r_i}$ and $\vec{r_j}$ are the position vectors of atoms i and j, respectively. The generalization of Voronoi analysis for multicomponent systems that is called radical plane method may also be preferred for geometrical characterization in which atomic radii of elemental species are also considered while determining the plane boundaries between atoms. In that case the position vector is,

$$\vec{r} = \frac{R_i \vec{r_i} + R_j \vec{r_j}}{R_i + R_j} \tag{2.24}$$

where R_i and R_j are atomic radii of atoms i and j, respectively.

2. Determining the normal vector:

$$\vec{n} = \vec{r_j} - \vec{r_i} \tag{2.25}$$

where $\vec{n}$ is the normal vector of the boundary plane.

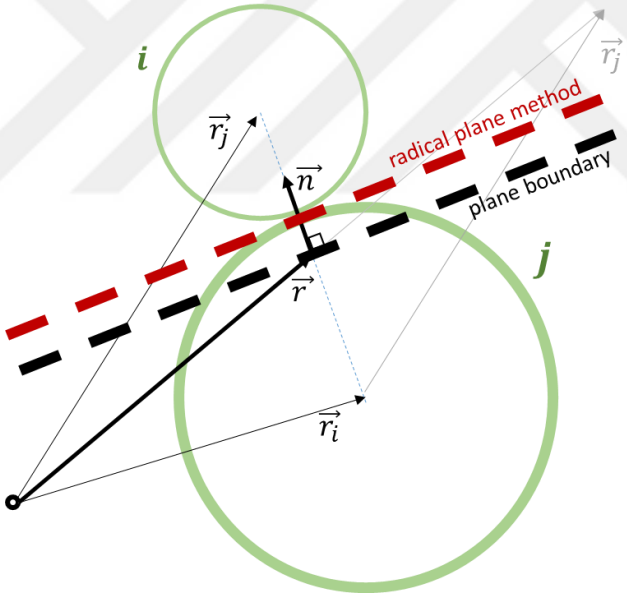

Figure 2.7 Geometric representation of the calculation of the plane boundary between two atoms.

In Figure 2.7, plane boundary calculation procedure was illustrated. Atoms i and j are of different species; thus having different radii. In the classical procedure this results in no difference. The normal vector and the position vector was determined so that

each point on the plane has equal distance to the central points of both atoms. On the other hand, since radical plane method also considers radii of atoms, the resulting plane boundary has been shifted through the smaller atom while its normal vector remains the same so that resulting plane has equal distance to the surface of the atoms, considering the atoms are of hard spheres.

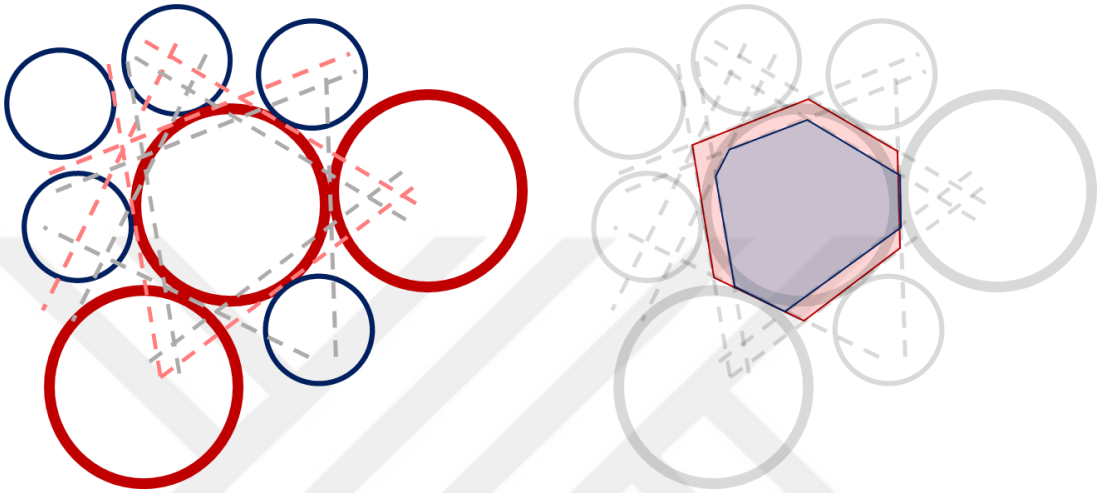

Figure 2.8 Illustration of Voronoi tessellation analysis in 2D.

In Figure 2.8, Voronoi tessellation of hard disks in 2D space was illustrated. On the left side, red and blue atoms represent the atoms of two different species having different radii. Light gray and light red dashed lines correspond to plane boundaries obtained by conventional and radical plane methods, respectively. On the right side, corresponding Voronoi cells are shown in blue (conventional) and red (radical plane). While in 2-dimensional space, Voronoi cells are of polygonal geometry; in 3D space they occur as polyhedrons.

In terms of computational geometry, the most feasible computational approach to calculate the Voronoi diagram of a space containing a number of points is to use plane sweep algorithms REF. This method returns the tessellation as a single object consisting of vertices and edges. However, this approach is not suitable for physical applications such as analyzing the atomic structure, it becomes unable to inspect each Voronoi cell. Therefore, another approach enabling individual computation and

analysis of each Voronoi cell corresponding a particle is necessary [103]. For this purpose, the following procedure is applied in order to compute the Voronoi cell of an individual atom:

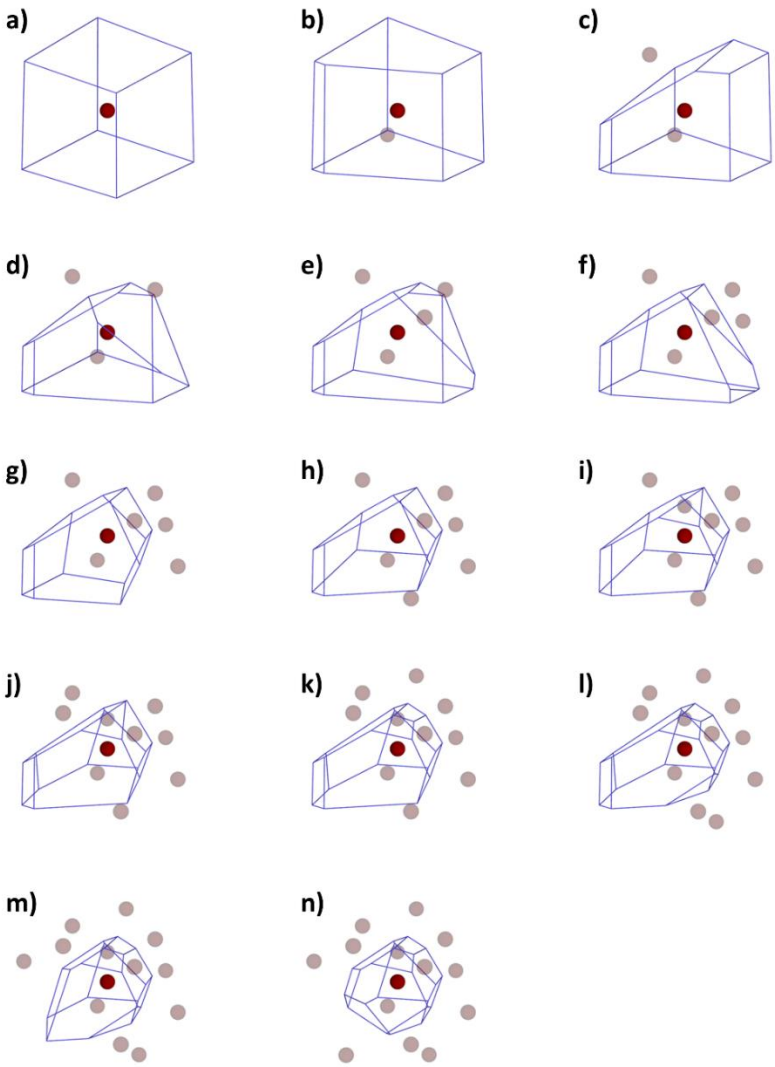

Figure 2.9 Construction of a Voronoi cell by cutting the initial polyhedron (cube) with plane boundaries and determination of neighboring particles forming an atomic cluster.

1. Compute the list of candidate neighbors that is the list of atoms having a distance lower than a cutoff distance.

2. Generate a cubic box as an initial form of the Voronoi polyhedron having an edge longer than the cutoff distance.
3. Compute the boundary planes and trim the Voronoi polyhedron by cutting with the boundary planes.
4. Determine the neighboring atoms as the atoms having boundary planes that constitute the faces of the final form of the Voronoi polyhedron.

In Figure 2.9a-n, the stages of the process of trimming the initial cubic box into the Voronoi polyhedron by the use of plane boundaries and consequential neighboring atoms are illustrated.

Thus, each atom in the space is represented by a Voronoi polyhedron. Since, each face of a polyhedron is the result of a plane boundary between two atoms, every single face of the polyhedron determines the border between the central atom and one of its neighboring atoms and the number of faces forming a polyhedron corresponds to the number of neighboring atoms (coordination number) of the corresponding atom. Each face is shared by two atoms, and the edges of these faces are shared by three atoms; therefore, the number of edges forming the face that is shared by an atom pair gives the number of common neighbors of the corresponding atom pair. All polyhedrons were defined by 5-digit Voronoi indices in the form of $<N_3\ N_4\ N_5\ N_6\ N_7>$ where each digit represents N_i number of i-edged faces.

The Voronoi polyhedra can be roughly separated into three categories: icosahedral-like, crystal-like and mixed [104]. Within these categories <0 0 12 0 0>, having 12 neighbors, each represented by N_5 (5-edged) faces, represents the nearly perfect icosahedral structure, <0 1 10 2 0> is a commonly observed icosahedral derivative, and <0 2 8 4 0> can be interpreted as either a highly distorted icosahedral-like or a mixed-type cluster. The <0 3 6 x 0> represents a common mixed-type cluster family, and clusters relatively dominated by N_4 (4-edged) and N_6 (6-edged) faces such as <0 4 4 6 0> are considered as crystal-like. By the use of these family of indices, minor structural transformations within disordered systems and structural heterogeneities in atomic scales are detected and interpreted. Additionally, statistical distribution of

volume of Voronoi cells and area of faces constituting the polyhedrons also provide useful information.

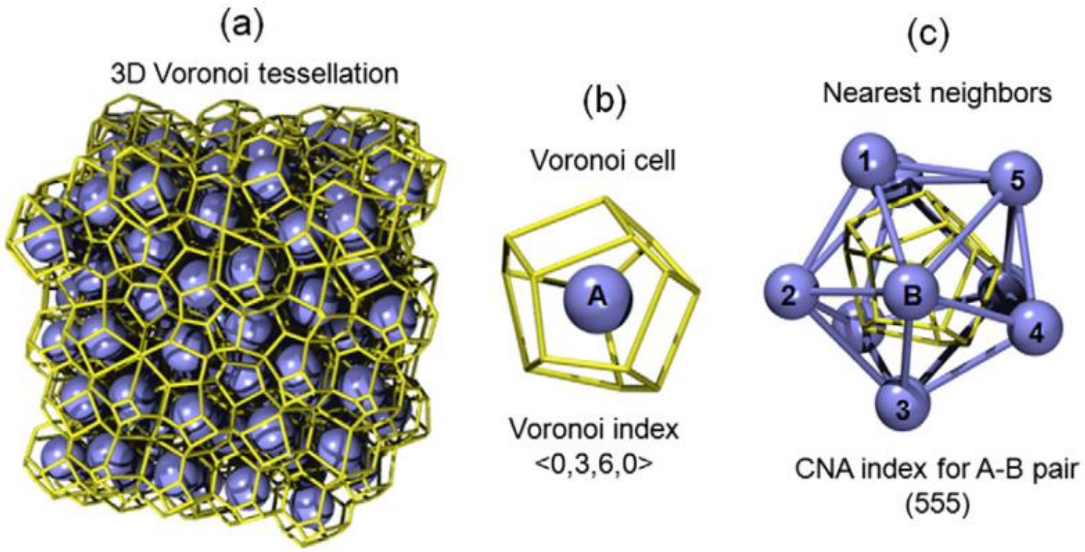

Figure 2.10 Illustration of Voronoi tessellation analysis and Common-neighbor analysis (CNA). (a) Voronoi tessellation of multiple atoms, (b) Voronoi polyhedron of the atom A, having three quadrilateral and six pentagonal faces, and (c) common-neighbor analysis of A-B atom pair, having five enumerated common neighbors that bond among each other as a loop structure [2].

2.2.3 Common-Neighbor Analysis

Common-neighbor analysis (CNA) [105] provides local geometric characterization of a neighboring atomic pair in a system. The characteristic CNA index of an atom pair is constituted by three integers jkl. j is the number of common neighbors of the atom pair, as in the number of edges of the face that is shared by a neighboring atomic pair in Voronoi tessellation. k is the number of bonds among common neighbor atoms, and l is the number of bonds that constitute the longest chain within of interatomic k bonds. Voronoi tessellation method and common-neighbor analysis are strictly related to each other; while the former characterizes an individual atom, the latter is related to an atom pair, although both contain very similar information. Both methods have been illustrated on the same atom in Figure 2.10.

Among crystalline structures, a fcc atom has 12 neighbor having CNA index of 421; a hcp atoms has six 421 neighbor and another six 422 neighbor; a bcc atom has eight 666 neighbor and six outer 444 neighbor [106]. In the atomic structure of disordered systems such as liquids and glasses, CNA index of 555 is commonly present, indicating the presence of icosahedral symmetry [2]. With the knowledge of these indices, crystal-like and icosahedral-like structures are able to be identified in disordered systems.

2.2.4 Honeycutt-Anderson Analysis

Honeycutt-Anderson (H-A) analysis [107] is very similar to common neighbor analysis. The H-A index is constituted by four integers: $ijkl$, where i indicates whether the two given atoms are directly bonded to each other or not. As in CNA, j is the number of nearest neighbors that is shared by these two atoms, and k is the number of bonds among the neighbors that is shared by the atom pair. The fourth integer l, is used to identify different bonding geometries while the first three integers of the H-A index are the same.

2.2.5 Coordination Number

Coordination number of an atom is the number of the nearest neighbors of an atom which are also considered the atoms bonded to the central atom. In crystals, coordination number usually defined as the atoms that are touching to each other while the atoms are considered as hard spheres. For example, coordination number of close-packed structures such as fcc and bcc is 12, while that of bcc and simple cubic, is 8 and 6, respectively.

On the other hand, the definition of coordination number in the disordered systems is fairly ambiguous. There are several options in order to determine the coordination number as illustrated in Figure 2.11 in 2D space [108]. One is the Voronoi tessellation method itself. Voronoi tessellation provides a method for parameterless determination of nearest neighbors; however, it should be decided whether to use the conventional or the radical method. Another common method is to use a cutoff radius. For

multicomponent systems cutoff radius may be determined for each component pair. In order to determine the cutoff radius, partial pair distribution functions are used. First minimum point after the first peak (shown in Figure 2.6 as a dashed line) can be considered as the average distance of the boundary that roughly separates the first and the second neighbor shells. The least common method is to use, n-closest neighbor method in which the coordination number is previously determined, and n number of closest atoms are assigned.

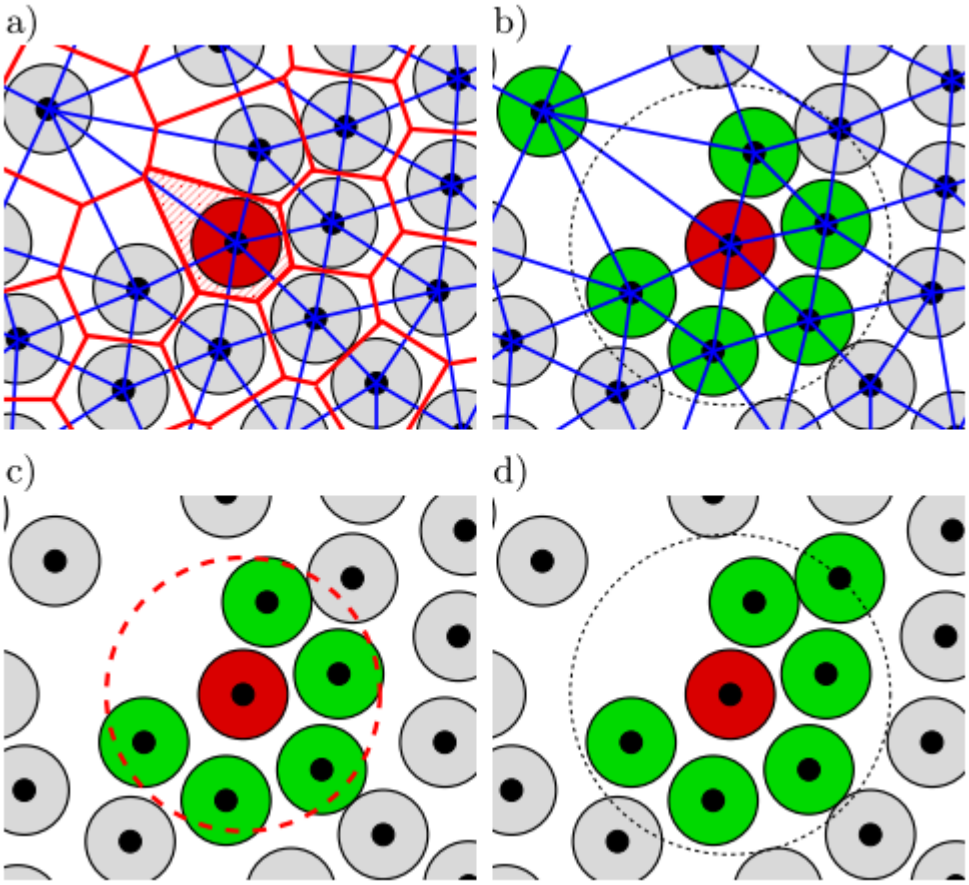

Figure 2.11 Commonly used nearest neighbor definitions: a) Voronoi tessellation method b) Delaunay triangulation, which is the dual of Voronoi tessellation method, c) cutoff radius, and d) n-closest neighbor method [108].

As seen in the above picture, the choice of nearest-neighbors is not unique, and the results of most of the topological characterization methods for disordered systems such

as common-neighbor analysis, Honeycutt-Anderson analysis, bond angle distribution, Warren-Cowley analysis, Cargill-Spaepen analysis, and bond-orientational order analysis are dependent upon the set of nearest neighbors of an atom.

2.2.6 Bond angle distribution

Bond angle distribution is a three-body correlation that provides bonding angle statistics of triplets of neighboring atoms. Once the nearest neighboring atoms of a central atom are determined with one of the methods described above, every the angle between each bond are calculated by the use of the law of cosines:

$$\theta_{ijk} = \cos\frac{r_{ij}^2 + r_{ik}^2 - r_{jk}^2}{2r_{ij}r_{ik}} \qquad (2.26)$$

where i is the central atom, j and k are the neighboring atoms, r_{ij} and r_{ik} are the length of ij and ik bonds (the distance between the central atom and neighboring atoms), and r_{jk} is the distance between two neighboring atoms j and k. The bond angle distribution function is defined as:

$$g(\theta) = \frac{1}{\sum_{i=1}^{N} N_i(N_i-1)} \sum_{i=1}^{N} \sum_{j=1}^{N_i} \sum_{k=j+1}^{N_i} \delta(\theta - \theta_{ijk}) \qquad (2.27)$$

Bond angle distribution function has only spikes for perfect crystals; for example it is only positive at 90° and 180° for simple cubic crystals, and 109° for diamond cubic crystals having tetrahedral symmetry [2]. In liquid and amorphous structures, the bond angle distribution function characteristically contain three broad peaks: The sharpest one has its center at acute angles, one at obtuse angles the, and the broadest resides close to straight angles. The variances of the peak position and broadness are interpreted as structural varieties.

2.2.7 Local Chemical Structure Analyses

For multicomponent systems, the analysis of chemical distribution of nearest neighbors is useful to detect chemical heterogeneities in atomic scales in disordered systems. These features provide further information when examining phase

transformation behavior and mechanical properties; dealing local chemical ordering behavior of a disordered system rather than treating the system as a homogeneous medium may further explain its extraordinary behaviors contradicting with conventional theoretical approaches depending upon macroscopic observations.

Warren-Cowley [109], [110] which is a parameter that exhibits the short-range deviations from the chemical composition of the system is defined as:

$$\alpha_{AB} = 1 - \frac{Z_{AB}}{x_B Z_A} \tag{2.28}$$

where Z_{AB} is neighboring B atoms around an A atom, Z_A is a coordination number of an A atom, and x_B is the fraction of the component B. If multiplication of coordination number and nominal composition of the solute atoms (B atoms) is equal to the partial coordination number that is the number of the neighboring solute atoms, then the Warren-Cowley parameter takes the value of zero, and the system is considered as a random solution. Positive deviation of the parameter indicates that A atoms tend to collect solute atoms around them.

Cargill-Spaepen parameter [111] similarly indicates the chemical deviation with a slightly different approach:

$$\eta_{AB} = (x_A Z_A + x_B Z_B)\frac{Z_{AB}}{x_B Z_A Z_B} - 1 \tag{2.29}$$

where Z_A and Z_B are the total coordination number around A and B atoms, respectively. Then, the term, $x_A Z_A + x_B Z_B$, indicates the average coordination number of all atoms. Z_{AB} is neighboring B atoms around an A atom, and x_B is the fraction of the component B, as in the definition of Warren-Cowley parameter. The maximum value of the Cargill-Spaepen parameter is the case of Z_{AB} and Z_A are being equal to eachother:

$$\eta_{AB}^{max} = \frac{x_A Z_A + x_B Z_B}{x_B Z_B} - 1 \tag{2.30}$$

The parameter, then, can be normalized against η_{AB}^{max}:

$$\eta_{AB}^{0} = \eta_{AB}/\eta_{AB}^{max} \tag{2.31}$$

The normalized η_{AB}^{0} can take values from 0 to 1; thus, become easier to be interpreted numerically. If η_{AB}^{0} is equal to zero, then the solution is completely random. Otherwise, if η_{AB}^{0} is equal to one; it means that A atoms are bonded with B atoms only.

2.2.8 Bond-Orientational Order

Bond-orientational order [112] is a set of many-body correlational parameters expressing local ordering mathematically by the use of spherical harmonics. This ordering parameter is only sensitive the bonding directions of the neighboring atoms and not the bond lengths [113]. In order to determine the bond-orientational order parameter of an atom; firstly, an intermediate value should be calculated for each bond:

$$Q_{lm}(\vec{r}) = Y_{lm}(\theta(\vec{r}), \phi(\vec{r})) \tag{2.32}$$

where $\vec{r}$ is position vector of neighboring atom with respect to the central atom, $\theta(\vec{r})$ and $\phi(\vec{r})$ are the spherical coordinates. Y_{lm} is a spherical harmonic function having degree of l and order of m:

$$Y_{lm}(\theta, \phi) = (-1)^{m} \sqrt{\frac{(2l+1)}{4\pi} \frac{(l-m)!}{(l+m)!}} P_{lm}(\cos\theta) e^{im\phi} \tag{2.33}$$

where P_{lm} is the associated Legendre polynomial:

$$P_{lm}(x) = \frac{(-1)^{m}}{2^{l} l!} (1 - x^{2})^{m/2} \frac{d^{l+m}}{dx^{l+m}} (x^{2} - 1)^{l} \tag{2.34}$$

After Q_{lm} is calculated for each neighboring atom, the average $\bar{Q}_{lm} = \langle Q_{lm}(\vec{r}) \rangle$ is taken over all neighbors. In general, nonzero averages are obtained for $l = 4$ in atoms having cubic local symmetry, and $l = 6$ in atoms having icosahedral local symmetry [112]. Since $\bar{Q}_{lm}$ is changed drastically change if the coordinate axes are rotated, the bond-orientational order parameters, Q_l, are defined as:

$$Q_{l}(\vec{r}) = \sqrt{\frac{4\pi}{2l+1} \sum_{m=-l}^{l} |Q_{lm}(\vec{r})|^{2}} \tag{2.35}$$

so that the resulting metrics are scalar and rotationally invariant [114].

Table 2. 1 – Values of Q_l for atomic clusters of perfectly symmetric body-centered cubic, face-centered cubic, hexagonal close-packed, icosahedral, and simple cubic configurations [108].

	bcc		fcc	hcp	icosahedral	sc
	n=8	n=14	n=12	n=12	n=12	n=6
Q2	0	0	0	0	0	0
Q3	0	0	0	0.076	0	0
Q4	0.509	0.036	0.19	0.097	0	0.764
Q5	0	0	0	0.252	0	0
Q6	0.629	0.511	0.575	0.484	0.663	0.354
Q7	0	0	0	0.311	0	0
Q8	0.213	0.429	0.404	0.317	0	0.718
Q9	0	0	0	0.138	0	0
Q10	0.65	0.195	0.013	0.01	0.363	0.411
Q11	0	0	0	0.123	0	0
Q12	0.415	0.405	0.6	0.565	0.585	0.696

In Table 2.1, the values of Q_l for various perfectly symmetric local configurations have been tabulated [108]. Positive values of bond-orientational order parameters indicate some form of local cluster ordering. The most commonly used bond-orientational order parameters in order to distinguish distinctive ordering characteristics are Q_4 and Q_6. Local variations and structural transformations such as glass transition and crystallization are detected by examining Q_4 vs. Q_6 plot of the system as shown in Figure 2.12.

The bond-orientational order parameters are also extended to the first neighbor shell by averaging the complex bond order vectors, Q_{lm}, over neighboring atoms [115]:

$$\bar{Q}_{lm}(i) = \frac{1}{N_b(i)} \sum_{k=0}^{N_b(i)} Q_{lm}(i) \qquad (2.36)$$

in which the sum from $k = 0$ to $N_b(i)$ runs over all neighboring atoms with the index of $k > 0$ and the atom i itself. Then, the extended bond orientational order parameter is similarly described as:

$$\bar{Q}_l(\vec{r}) = \sqrt{\frac{4\pi}{2l+1}\sum_{m=-l}^{l}|\bar{Q}_{lm}(\vec{r})|^2} \tag{2.37}$$

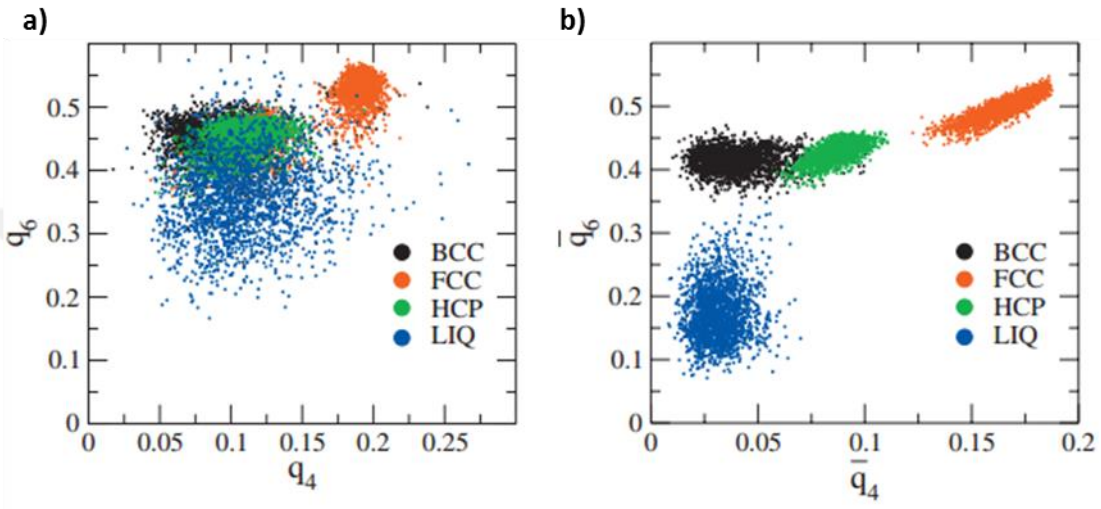

Figure 2.12 Comparison between conventional (Q_4 vs. Q_6) and extended ($\bar{Q}_4$ vs. $\bar{Q}_6$) bond orientational order parameters of systems of 2000 atoms having bcc (black), fcc (red), hcp (green) and liquid (blue) phases [115].

As seen in Figure 2.12, using extended bond-orientational order parameters rather than using regular bond-orientational order parameters provide more accurate differentiation between crystalline structures; since, the overlapping regions of different phases in $Q_4 - Q_6$ plane decrease significantly.

CHAPTER 3

STRUCTURAL MODELING OF LIQUID AND AMORPHOUS Al91Tb9 BY MONTE CARLO SIMULATIONS

Formation of the topological and chemical inhomogeneities within the $Al_{91}Tb_9$ marginal metallic glass system during vitrification was investigated by the use of Monte Carlo (MC) simulations. The interatomic potential for Al-Tb binary system was developed using experimentally obtained structure factor of liquid and atomic configurations of liquid and amorphous phases from 1200 K to 300 K were obtained. Voronoi Tessellation method and chemical short-range order analysis by computing the Warren-Cowley parameter have revealed a substantial degree of compositional inhomogeneity at nanoscopic scales consisting of pure aluminum islands which were found to dominate the system as the temperature decreases with increasing size and number, especially in supercooled liquid region. These pure aluminum structures are thought to be the reason of high number density of primary aluminum nanocrystals; therefore, they have been called as prenucleation clusters.

3.1 Literature Review

Marginal glass forming alloys have been regarded as promising structural materials due to their nanocrystalline embedded glass-matrix composite structure due to their ability to form very high number density of nanocrystals upon devitrification [19, 20]. Unlike bulk metallic glasses, marginal glass formers, necessitate very high cooling rates ~10^6K/s in order to form a completely amorphous microstructure [21–23]. Low density high-strength Al-RE based alloys [116] and Fe-RE (RE: Rare-earth element) based soft and hard magnetic alloys [118] are two widely known examples for marginal glass formers. The crystallization process of marginal metallic glass formers

frequently results in very high number densities of crystals (10^{21}-10^{24} m^{-3}) having sizes of smaller than 50 nm. A wide ranging investigation on this phenomenon has still been resumed in order to explain for the mechanism underlying the formation of such high density of nuclei accurately. As the vast majority of bulk metallic glasses do not produce nanocrystals when similar crystallization procedures are applied; the solution for this puzzling behavior may be hidden at the atomic structure of the marginal glass forming alloys quenched from liquid.

The former studies on Al-RE and Al-RE-TM (TM: Transition metal) amorphous alloys have resulted in two main conjectures on the formation of high density of nanocrystals after annealing at low-temperature. The first theory claims that there already exists a small fraction of crystalline nuclei in the as-quenched glass [121]. The growth of these nuclei is extinguished by sudden increase in the viscosity and kinetic freeze as the glass transition temperature (T_g) is surpassed during rapid cooling. Therefore the newly formed nuclei having size of sub-nanometers which cannot be detected my diffraction experiments are trapped in the glass matrix and subsequent low-temperature annealing below T_g results in the growth of these "quenched-in nuclei". This hypothesis was tested by comparing Al-Sm metallic glass samples produced by melt spinning and cold rolling [121]. The presence of highly populated fcc-Al nanocrystals, which were detected in melt-spun specimens, was not reported in the cold-rolled specimens undergoing similar heat treatment processes. In addition, fluctuation electron microscopy peaks [122] which indicate that the existence of a medium-range order (MRO) structure for Al atoms resembling fcc crystal structure in the melt-spun specimen were not present in the cold-rolled alloy. This observation is in harmony with the hypothesis of the presence of fcc-Al nuclei frozen within the matrix during rapid cooling of the as-spun ribbons. There exists a separate type of atomic arrangement in which fcc-like medium-range order is missing in cold-rolled specimens in which the amorphization process is completely different.

The second theory is based on phase separation [23, 26] developing in the glass matrix by a mechanism analogous to spinodal decomposition [123]. The origin of the phase-

separation was explained through a time-independent homogeneous nucleation theory which is called coupled-flux nucleation [26, 27]. According to this argument, glass phase that is resulted by rapid cooling is separated into Al-rich and RE-rich regions before crystallization. Al-rich isolated regions which has approximately size of 100 nm [120] are thought to be responsible for the formation of fcc-Al nanocrystals. Both hypotheses were debated in terms of different aspects [28–30]. For example, the phase separation which was observed in $Al_{88}Gd_6La_2Ni_4$ [123] alloy system is not reported for $Al_{88}Gd_6ErNi_4$ [127]. Furthermore, a two-stage route for primary crystallization of fcc-Al was suggested for several Al-TM-RE marginal metallic glass systems which does not agree with "quenched-in nuclei" proposition [128].

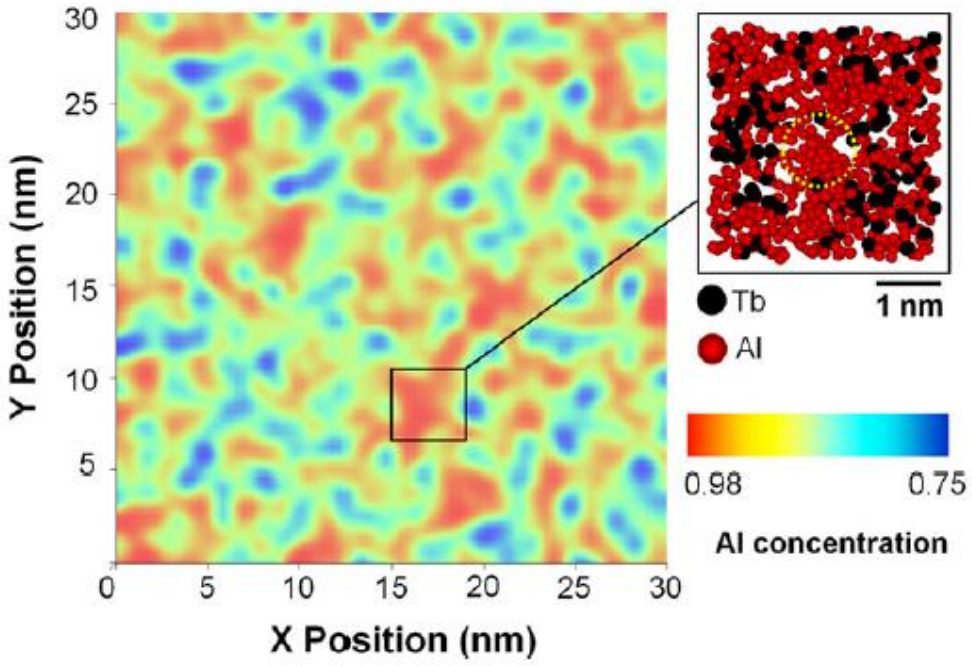

Figure 3.1 2-D Al concentration map over 30x30x4 nm volume of data for as-quenched $Al_{90}Tb_{10}$. Inset (right corner) shows 3-D APT results over a volume of 4x4x2 nm indicating cluster of pure Al (circled). The color bar (left corner) indicates the concentration limits. Adapted from [126].

Lately, it has been presented that the phase separation in Al-RE systems may actually be present at nanoscopic scales in the as-quenched glass structure [23, 26–30, 33] as

well as in other systems such as Fe-based, Pd-based and Zr-based metallic glasses [130]. Kalay et al. have proved the existence of pure aluminum regions having size of 1 nm in as quenched $Al_{90}Tb_{10}$ by the use of atom probe tomography (APT) [126]. It was calculated that these regions have an approximate number density of 10^{25} m^{-3}. APT data gathered from the samples show that heat-treatment at temperatures just below the crystallization temperature results in the coalescence of pure Al regions reducing the number density of pure aluminum clusters to 10^{21-22} m^{-3}. Small angle X-ray scattering (SAXS) studies show that there occurs a phase separation in some other Al-RE amorphous alloys such as $Al_{91}Tb_9$ prior to crystallization [131]. According to SAXS/WAXS measurements, the further coalescence of these chemical fluctuations eventually leads to the formation of primary fcc-Al nanocrystals [36, 37]. According to fluctuation electron microscopy (FEM) studies applied on both as-quenched and annealed samples of Al-RE alloys evidently reveal medium-range order to a certain extent. Consequently, the phase-separated Al and RE rich regions may possess their own atomistic structure originally in the as-quenched state. While these structures do not have conventional crystallographic symmetries, they still hold medium-range correlations.

While previously mentioned experimental approaches are able to detect the microstructural features only after the phase separation has occurred, the process of formation of these features can only be investigated by the use of suitable techniques at the moment. In this study, by examining the short to medium range topological and chemical correlations, a possible kinetic pathway for the chemical and topological evolution of pure aluminum regions was investigated during vitrification of $Al_{91}Tb_9$ alloy. The role of these regions as prenucleation clusters enabling the nucleation of high density fcc-Al nanocrystals by the use of Monte Carlo (MC) simulations.

3.2 Experimental Procedure

The $Al_{91}Tb_9$ alloy ingots have been produced by electric arc-melting under argon atmosphere by using highly pure aluminum (99.99 wt%) and terbium (99.9 wt%) precursors. The diffraction experiments on molten $Al_{91}Tb_9$ were previously performed

by using the high-energy X-ray diffraction (HEXRD) at the Advanced Photon Source at Argonne National Laboratory. Samples for molten $Al_{91}Tb_9$ analysis were cast into 2 mm diameter rods by the use of suction casting. The rods were inserted into quartz capillary tubes and sealed under argon atmosphere. Capillary tubes were lined with carbon in order to prevent the contamination of the liquid alloy by lowering the interaction of quartz at high temperatures. The capillary tubes were heated up to 1208 K and exposed to 100 keV of radiation which corresponds to a wavelength of 0.124 Å. The diffraction data obtained from the liquid were collected in transmission (Debye-Scherrer) geometry by the use of a MAR charge coupled device (CCD) having 60 seconds of exposure time. Similar diffraction patterns were collected from the holder and empty capillary tube in order to eliminate background features. The raw HEXRD data obtained from the molten alloy were also corrected for polarization, absorption, multiple, Compton scattering and converted to the total structure factor function, S(Q) by following the procedure described in [129].

The ab-initio Molecular Dynamics (AIMD) simulations were performed by using Vienna ab-initio Simulation Package (VASP). Periodic boundary conditions were employed, and NVT ensemble has been used. Nosé-Hoover thermostat is also utilized in order to control temperature and pressure [38–41]. Initial number densities for $Al_{91}Tb_9$ was estimated by using linear combination of pure Al and Tb elements. The exchange–correlation functional was approximated by generalized gradient approximation (GGA) by using Perdew–Burke–Erhzernhof formulations. 200 atoms having the same stoichiometry with produced alloys were generated in a periodic cell with random distribution. In the beginning, the system temperature was increased up to 2500 K in order to cancel out the effects of initial particle distribution and obtain an unbiased liquid configuration. Then, the system temperature was gradually decreased to 1208 K and finally to 300 K.

Reverse Monte Carlo (RMC) simulations were conducted by using RMC++ simulation package [138] in order to obtain partial pair distribution functions of liquid $Al_{91}Tb_9$ based on experimentally obtained diffraction data. Since the experimental data only

consists of the total structure factor which can be converted to total pair distribution function, the RMC simulation was constrained using the density and the partial pair distribution functions from the AIMD simulation in order to obtain realistic partial distribution functions that can reproduce the experimental data [2, 42] . The comparison of the reproduced and experimental structure factors can be seen in Figure 3.2a. The use of RMC associated with partial pair distribution functions obtained AIMD, produces partial pair distribution functions having longer ranges which cannot be obtained by solely AIMD simulations because of the limited number of particles [139].

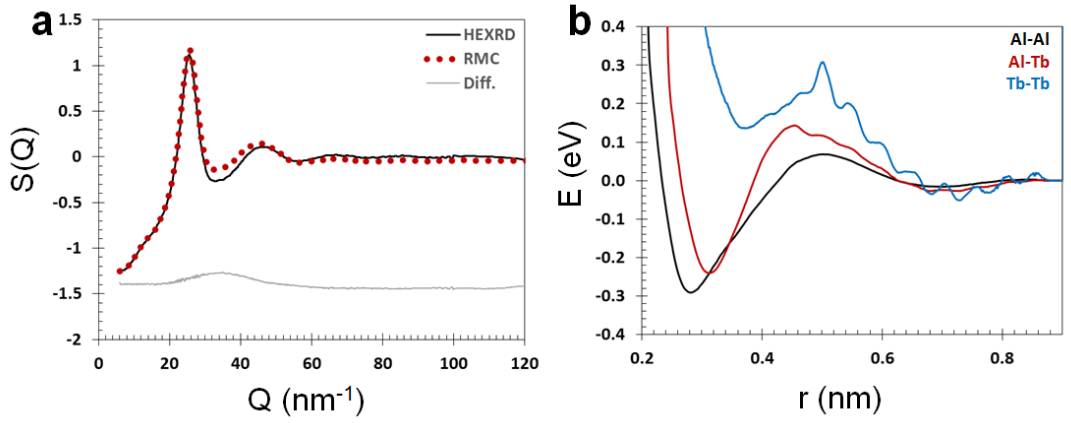

Figure 3.2 (a) Structure factor function, S(Q), data retrieved from high energy X-ray diffraction experiment (black line), and reverse Monte Carlo simulation (red-dotted line), (b) the interatomic pair potential functions developed by the use of inverse Monte Carlo algorithm [7].

After a reliable atomistic model of $Al_{91}Tb_9$ liquid with 20,000 particles have been produced, Inverse Monte Carlo (IMC) [56] was used in order to develop an interatomic potential representing the Al-Tb system at related composition. Partial pair distribution functions acquired from RMC were used as a target configuration in the IMC algorithm. Firstly, the system was initiated with a random configuration and estimated interatomic potentials. As the algorithm proceeds the interatomic potentials have been

evolved in order to attain the target atomic configuration which is designated by the partial pair distribution functions obtained from RMC.

Monte Carlo simulations were made at constant number of particles, volume and temperature (NVT ensemble) by the use of interatomic potentials that had been developed. Initially, $Al_{91}Tb_9$ system of 32,000 atoms was initialized in fcc configuration and equilibrated for 100,000 steps at 1200 K in order to reach a relatively stable state.. Temperature of the system was decreased 100 K at each simulation stage up to room temperature (300 K), while the volume of the system was taken from AIMD simulations for each stage. At subsequent stages, the starting atomic configuration for a stage is taken from the ultimate configuration of the previous one, and then equilibrated for 50,000 steps which is sufficient for the energy minimization. After the equilibration is complete, the structural data was collected for 5 sets between intervals of 1,000 steps. Source code for Monte Carlo simulation and structural analysis techniques is available at an online repository [148].

3.3 Results and Discussion

The pair potential functions that were constructed by the use of IMC are seen in Figure 3.2b. The interaction of terbium atoms among themselves was represented restrictedly resulting the noisy behavior of E(r)-r curve. However, the pair distribution functions retrieved from Monte Carlo simulation at 1200 K using these pair potentials, sufficiently fits with partial pair distribution functions collected from the RMC simulation (red-dotted line) as seen in Figure 3.3a-c. Therefore, it is believed that the pair potentials developed by the use of IMC algorithm represent the Al-Tb pair interactions successfully. Evolution of partial pair distribution functions obtained from isothermal MC simulations from 1200 K to 300 K was shown in Figure 3.3a-c. It can be conceived from the rapid decrease in the rate of change of the average atomic volume with respect to temperature in AIMD simulation and that of corresponding MC simulations that was given in Figure 3.4a that the system encounters a glass transition near 600 K.

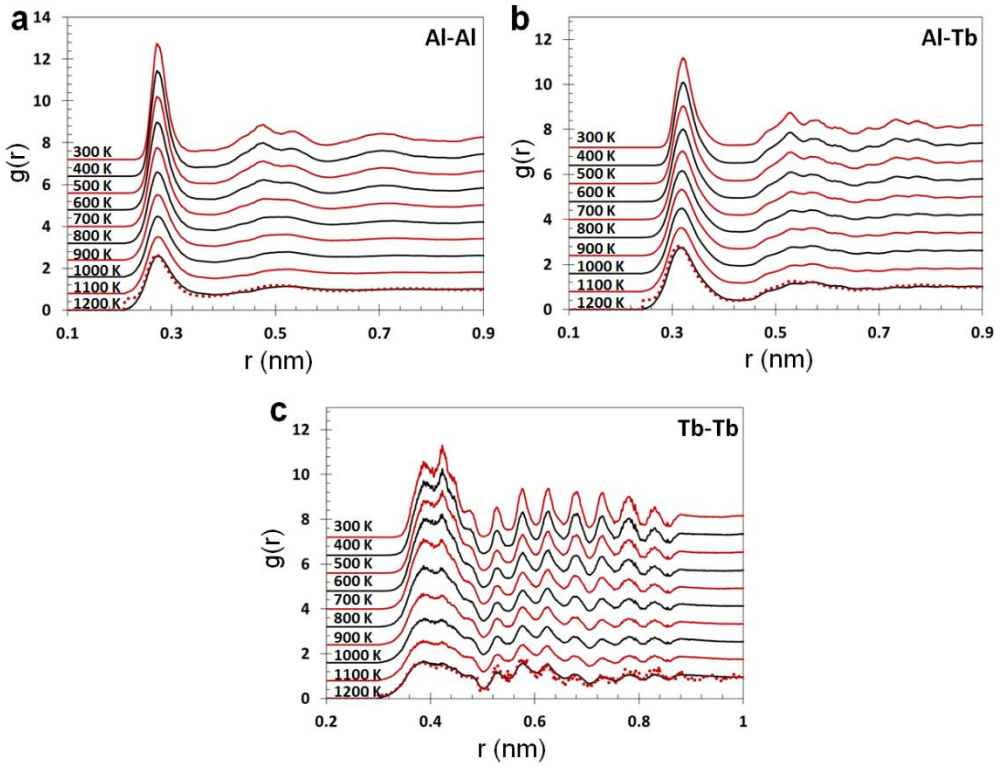

Figure 3.3 Development of partial pair distribution functions, g(r), of (a) Al-Al, (b) Al-Tb, and (c) Tb-Tb atomic pairs with respect to temperature obtained from Monte Carlo simulations and comparison with partial pair distribution functions at 1208 K retrieved from reverse Monte Carlo (red-dotted line) [7].

The change in the local atomic structure of aluminum-centered clusters was firstly examined by the use of Voronoi Tessellation [129]. The number of some aluminum-centered clusters appreciably increases during vitrification as shown in the Figure 3.3b which is the initial sign of a degree of ordering. In Figure 3.4b, Voronoi indices of populous aluminum centered clusters were shown. Icosahedaral-like clusters like <0 0 12 0 0> and <0 1 10 2 0> abruptly dominated the system near the glass transition, and <0 3 6 4 0> clusters becomes more preferred with a constant increase in population with decreasing temperature, and <0 2 8 4 0> clusters display a change in between. The population of crystal-like <0 4 4 6 0> clusters increase slightly in the amorphous

state, however some other populated clusters that are present in the liquid phase such as <1 2 6 3 1>, <0 3 6 3 0>, and <1 3 4 5 1> do not show a noticeable difference in number throughout the vitrification process. It should be noted that the populated aluminum-centered clusters were primarily seen to be based in aluminum-rich regions. Aluminum-centered clusters in Terbium-rich regions have mostly irregular shapes irregularly and there is not a dominant type of cluster within these regions. There is no definite type of clustering observed in liquid for terbium-centered clusters; however, <0 2 8 x 0> and <0 1 10 x 0> cluster groups were observed to emerge with decreasing temperature, as shown in Figure 3.4c. The <0 1 10 x 0> clusters are attributed to icosahedral-like configuration that is frequently observed in amorphous structure. The <0 2 8 x 0> clusters may also be a signature of an additional ordering within terbium-rich regions antecedent for metastable intermetallics. Terbium-rich regions have a configuration such that terbium atoms are predominantly enveloped by aluminum atoms and these atomic pairs are located so that there is a specific distance with respect to each other forming a network structure, because of the high attraction between aluminum and rare-earth atoms as shown in the previous studies and the current one [129]. This structural character is also very parallel to the associated intermetallic compounds of the Al-Tb system such as Al_3Tb trigonal (SG:R-3m) structure and metastable $Al_{17}Tb_2$ (SG:P63/mmc) hexagonal structure. Furthermore, the peak appeared at 0.42 nm in Tb-Tb partial pair distribution function (Figure 3.3c) due to splitting of the first shell peak also corresponds to the closest Tb-Tb distance of trigonal Al_3Tb intermetallic crystal. This sort of quasi-periodic ordering may also be the configurational source of the pre-peak that was examined in diffraction patterns of certain glasses that is also called as the first sharp diffraction peak [140]. The so-called "superatoms" [126], rare-earth centered clusters between the highly pure Al regions is believed to be responsible for a strong pre-peak frequently observed in Al-RE marginal glass forming alloys [28–30, 33]. The previous studies with $Al_{90}Sm_{10}$ marginal glass forming alloys, some medium range order structure corresponding to a high-temperature metastable tetragonal $Al_{11}Sm_3$ (SG:I4/mmm) were detected by the use of HEXRD experiments and RMC simulations [129]. Similarly, using fluctuation

electron microscopy (FEM), MRO of pseudo-trigonal Al_3Tb was highlighted for as-quenched $Al_{90}Tb_{10}$ alloy [126]. The overall structural progression is consistent with the Frank's hypothesis [141] advocating that the preeminence of energetically favorable icosahedral-like structures having no translational symmetry constrains the crystallization of the system.

Warren-Cowley parameter have been calculated in order to detect the chemical inhomogeneities within the short range [47, 48]. Figure 3.5a shows the fraction of Al atoms belonging to pure-Al clusters and the average number of atoms within these clusters calculated by the use of Warren-Cowley short range order analysis [47, 48]. According to this analysis, the degree of Al-Al clustering has increased deliberately at temperatures lower than the glass transition temperature. Moreover, appreciable number of aluminum-centered clusters with Warren-Cowley parameters equal to 1 has been found for the center atom as well as all of the neighboring aluminum atoms. This apparently reveals the fact that the aluminum atoms are isolated so that they formed pure regions of aluminum exceeding the first-shell neighboring distance and supports the assumption that pure aluminum regions developed in MRO scale.

Pure aluminum clusters have been identified as regions of aluminum atoms having solely aluminum atoms as neighbors in first two neighboring shells. These regions that have been found to have number densities in the order of 10^{25} m^{-3} and their average size are of 100-200 Al atoms. These findings are in correlation with the observations made in the previous studies using atom probe tomography experiments [23, 29] indicating the presence of a network of rare-earth centered clusters that are interconnected to each other. This network separates pure Al regions; these regions has an average size of 1 nm in $Al_{90}Tb_{10}$ system and less than a nanometer in $Al_{88}Y_7Fe_5$ glass.

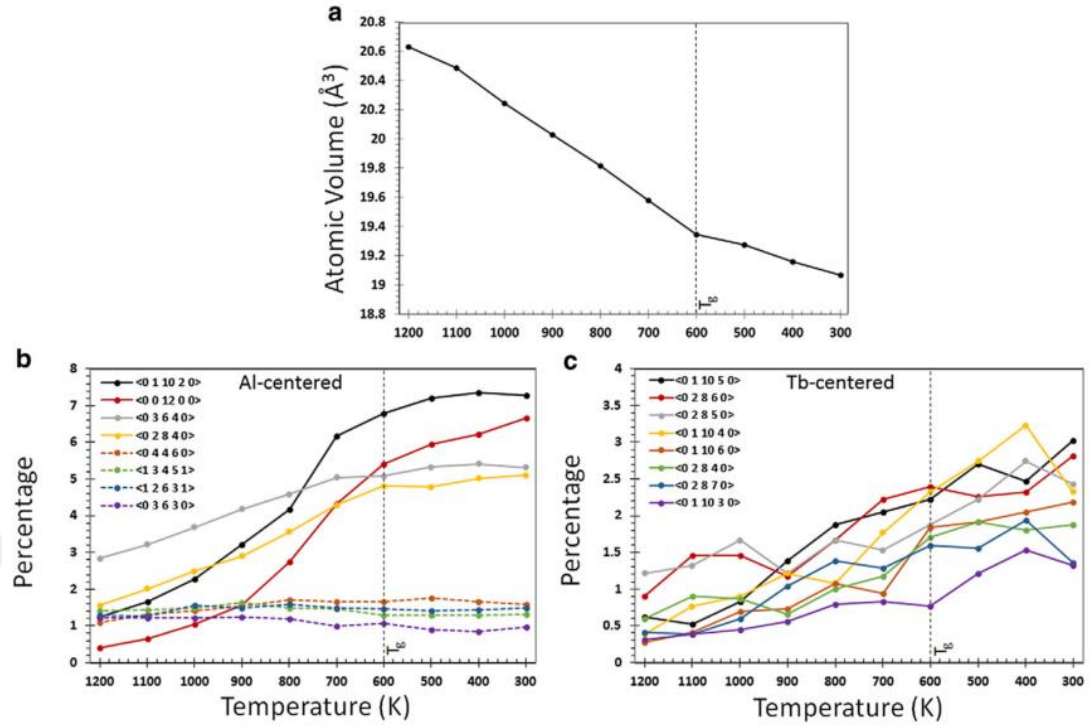

Figure 3.4 (a) Average atomic volume obtained from ab-initio molecular dynamics simulations and corresponding Monte Carlo simulations at various temperatures and the evolution of the population of chosen Voronoi indices of (b) aluminum-centered and (c) terbium-centered clusters [7].

According to the results of previously made atom probe tomography experiments and current Monte Carlo simulations, it is assumed that the network of rare-earth centered clusters and pure regions consisting of Al atoms that is present in the glass may form a MRO structure having some crystal-like periodicity which causes the first sharp diffraction peak at smaller angles of the diffraction pattern. It is worth to note that the same pre-peak with a lower intensity is also present in the liquid phase [129]. This is experimentally evident to a similar clustering behavior at a lower degree in the liquid at high temperatures. Therefore, the liquid is also inhomogeneous in terms of local atomic configuration. The presence of pure Al clusters in the liquid phase and their evolution from the molten liquid to amorphous that is observed in the current Monte Carlo simulations is consistent with the previous APT and diffraction experiments [29, 33]. As the temperature decreases, the ratio of aluminum atoms belonging to the pure

Al regions to the total number of aluminum atoms and the average size of individual regions increase, as shown in Figure 3.5a. Moreover, the growth these regions accelerates as getting closer to the glass transition temperature and it ceases after the glass transition because of the kinetic freeze.

In the previous studies on similar Al-based marginal metallic glass systems, critical size for nucleation for primary fcc-Al phase was calculated as approximately 90-120 atoms [23, 50]., The spatial domination of pure aluminum clusters with decreasing temperature is shown in Figure 3.5b-e. The clusters are colored with respect to their size such that as the size increases the color of the cluster approaches to red while smaller clusters are shown as gray. The color contrast was adjusted so that the clusters exceeding the critical nucleation size of fcc-Al nanocrystals was emphasized. The clusters having the size which is above have number densities on the order of 10^{25} m^{-3}. The clusters are trapped in the amorphous state and they are isolated from each other by the network of interconnected rare-earth clusters. Since the large rare-earth atoms decrease the diffusion rate, the interrupted growth of fcc-Al nanocrystals during the initial phase of devitrification is believed to be related to the low rate of long-range diffusion within the network of rare-earth clusters [143] The presence of isolated pure-Al clusters with such number densities results in the formation of aluminum nanocrystals with number densities of 10^{21}-10^{24} m^{-3} which is against the classical theory of nucleation as the amorphous phase is treated as a homogeneous medium.

The breakdown of classical behavior of nucleation was also observed in other systems. Lately, Wallace et. al. [144] proved the presence chemical inhomogeneities in liquid, and consequently and resulting in non-classical nucleation behavior occurs due to development of prenucleation clusters. The result of this Monte Carlo study combined with previous atom probe tomography and diffraction experiments [29, 33] explains the origin of another case of non-classical nucleation. The simulation results show that the chemical separation in the solid state may also be present in the liquid parent phase. During devitrification, the nanoscale chemical heterogeneity is responsible of (i) pure-Al regions acting as prenucleation clusters; (ii) these prenucleation clusters are

potential sites for nucleation of fcc-Al nanocrystals; (ii) rare-earth concentrated network surrounding these nanocrystals behaves as a barrier of diffusion because of its depressed atomic mobility and suspends the growth of fcc-Al nanocrystals [145], and consequently, (iv) results in the formation of high number densities of nanocrystals.

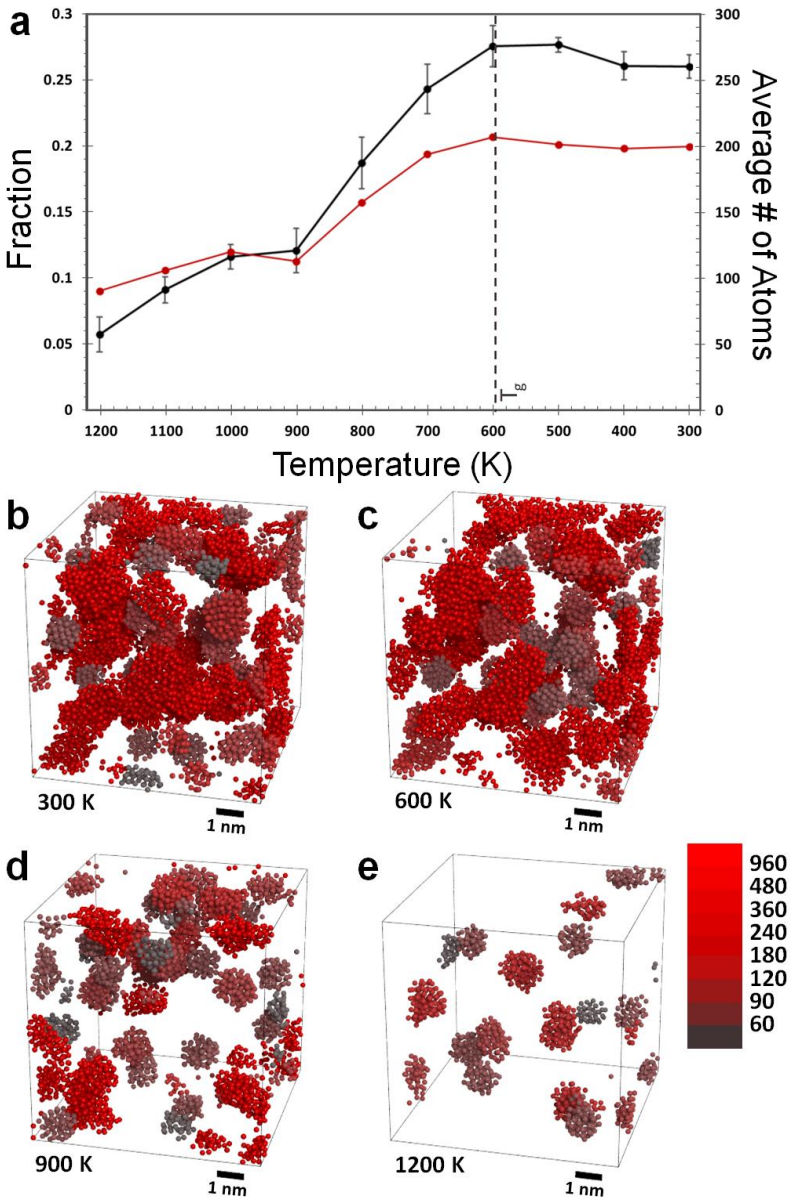

Figure 3.5 (a) Fraction of aluminum atoms belonging to pure aluminum clusters (black), and average cluster size as average number of atoms per cluster (red) obtained

from Monte Carlo simulations. The temperature of glass transition (T_g) was shown as a vertical dashed line. Size and spatial distribution of pure aluminum clusters at (b) 300 K, (c) 600 K, (d) 900 K, and (e) 1200 K. The cluster sizes are color-coded as number of atoms according to the color scale given at right [7].

3.4 Conclusion

In conclusion, the ambiguous behavior causing the formation of extremely high numbers of fcc-aluminum nanocrystals during the first stage of the devitrification of Al-RE metallic glasses is beyond the limits of the classical theory of nucleation. Development of aluminum-centered icosahedral-like clusters into pure aluminum prenucleation clusters near glass transition is concluded to inhibit crystallization of fcc-Al during vitrification while they act as nucleation sites during the structural relaxation of the system. According to previous atom probe tomography and current Monte Carlo results, it was hypothesized that the special extraordinary of terbium atoms or other rare-earth species with aluminum atoms within the molten liquid results in chemical separation as terbium and aluminum rich regions at nanoscale. While the network of rare-earth clusters breaks the matrix down into nanoscopic regions of pure aluminum isolated from each other where the crystallization is not possible during rapid cooling. The as-quenched amorphous phase consists of similar chemically separated regions having larger sizes. Our conclusion on pure-Al prenucleation clusters based on chemical and structural analyses on MC simulations coupled with diffraction studies are consistent with the recent similar experimental findings on $Al_{90}Tb_{10}$ amorphous system by the use of APT and explain the structural origins of these chemical inhomogeneities in parental liquid at high temperatures.

CHAPTER 4

CONCLUSION AND FUTURE RECOMMENDATIONS

4.1 Conclusion

In this thesis study, local atomistic structural order of Al-Tb alloy in amorphous and liquid states and its effects on the crystallization pathway during devitrification have been investigated by the use of computer simulation techniques, and the gap between atomistic modelling techniques and previous experimental studies have been bridged in order to illuminate the devitrification behavior of the system which cannot be explained by the classical nucleation theory.

Atomistic modelling techniques that are present in literature have been developed. Firstly, the inverse Monte Carlo algorithm has been implemented for binary systems in order to construct interatomic pair potentials from data obtained from diffraction studies. Then, classical Monte Carlo technique for NVT ensemble using periodic boundary conditions has been implemented. Several structural analysis tools that can be used simultaneously in conjunction with atomistic simulation techniques including have also been developed in order to make local atomistic structural characterization from atomistic configurations obtained from simulations. These tools consist of the calculation of partial pair distribution functions, bond angle distribution, Voronoi tessellation analysis, coordination number, Warren-Cowley chemical short range order analysis and bond-orientational order analysis.

Finally, the abovementioned computational tools have been applied to $Al_{90}Tb_{10}$ alloy. Initially, interatomic pair potential functions that are able to represent the Al-Tb system has been developed by using the inverse Monte Carlo algorithm. The input for this algorithm was the diffraction data of $Al_{90}Tb_{10}$ at 1208 K collected from HEXRD

experiments. The resulting interatomic potentials were successfully model the system at the temperature that experiment was conducted; the partial pair distribution functions obtained from the simulations were highly similar to those obtained from the experiment. Then, by using these interatomic potentials, the vitrification of $Al_{90}Tb_{10}$ from 1200 K to 300 K have been studied using Monte Carlo technique. Finally, evolution of the atomistic structure of the system throughout the vitrification process was characterized. Local clustering of atoms have been identified by the use of Voronoi tessellation. This method also enabled a robust determination of neighboring atoms. Warren-Cowley chemical short range order analysis have been identified the local deviations from the chemical composition by the consideration of neighboring species. It has been shown that chemical segregation at nanoscopic scales are already present in the liquid and the extent of aluminum and terbium-rich domains continuously increase throughout the vitrification. As a result, pure aluminum regions exceeding the critical size for nucleation of fcc-Al phase are formed during glass transition. While the crystallization within these regions is kinetically unable during rapid solidification, it is hypothesized that they act as potential nucleation sites during devitrification. As the presence of these regions increase the nucleation rate, the solute-rich network surrounding them suppresses the growth of initially formed nanocrystals giving rise to a non-classical nucleation behavior. For this reason, these regions consisting of only aluminum atoms have been called as “prenucleation clusters”.

4.2 Future Recommendations

This scope of this study is to make a topological analysis and to construct a reliable model that is consistent with structural investigations based on previous high-energy diffraction studies. However, further investigations based on energy calculations has to be made in order to have an extensive comprehension of the formation of these prenucleation clusters their effect on the thermodynamic barrier of nucleation. Finally, numerical calculation of the nucleation rate may become possible.

Inverse Monte Carlo algorithm provides only two-body interatomic potentials within a system which are unable to capture many-body interactions. Therefore, while these

potential functions represent the topology of the systems, they are unreliable for making energy calculations. Mendelev et. al. [146] have been developed a semi-empirical EAM potential for $Al_{90}Sm_{10}$ system by combining DFT simulations, empirical properties such as cohesive energy and elastic constants of crystalline species, and diffraction studies. Similar type of interatomic potentials should also be developed for the other Al-RE systems and compositions.

Once an energetically reliable interatomic potential is made, calculation of the energy barrier for nucleation would become possible for various amorphous configurations having various types of prenucleation clusters. However, nucleation process takes a very long time as compared with time ranges that the computer simulations can be performed. For this reason, processes such as nucleation are called as "rare events" in solid-state modelling: The events that are unfeasibly infrequent to be modelled. In order to model these events, a bias that will trigger the event should be applied to the system. Therefore, a reaction coordinate should be determined such that as the system is pushed through the reaction coordinate, the event will occur.

Bond-orientational order parameters have been used as a reaction coordinate for the nucleation process. Frenkel et. al. [147] studied the rate of homogeneous nucleation in a Lennard-Jones system. They have determined the nucleation barrier by the use of umbrella sampling, which enables the sampling of inaccessible configurations due to low overcoming probability of energy barriers in Monte Carlo simulations. They have also calculated the rate of nucleation by the use of molecular dynamics combined with the so-called technique of "blue-moon ensemble". In this technique, the molecular dynamics simulation is constrained so that the system is kept at the top of the nucleation barrier. This is made possible by mapping the nucleation barrier with respect to the reaction coordinates which are chosen as bond-orientational order parameters, and then biasing the system so that bond-orientational order parameters will take values that maximize the energy. When the system at the top of the nucleation barrier is relaxed, it goes forwards (crystallization occurs) or backwards (nuclei

dissolves). By repeating this procedure several times, forward and backward reaction rates are able to be computed.

This technique should also be applied to real systems such as Al-RE marginal metallic glass systems where the nucleation process is highly unconventional.

REFERENCES

[1] W. KLEMENT, R. H. WILLENS, and P. O. L. DUWEZ, "Non-crystalline Structure in Solidified Gold-Silicon Alloys," *Nature*, vol. 187, no. 4740, pp. 869–870, Sep. 1960.

[2] Y. Q. Cheng and E. Ma, "Atomic-level structure and structure–property relationship in metallic glasses," *Prog. Mater. Sci.*, vol. 56, no. 4, pp. 379–473, May 2011.

[3] M. Telford, "The Case for Bulk Metallic Glasses," *Mater. Today*, vol. 7, no. 3, pp. 36–43, 2004.

[4] A. Inoue, "Stabilization of Metallic Supercooled Liquid," *Acta Mater.*, vol. 48, pp. 279–306, 2000.

[5] L. Hu, X. Bian, X. Qin, Y. Yue, Y. Zhao, and C. Wang, "Thermodynamic basis for cluster kinetics: Prediction of the fragility of marginal metallic glass-forming liquids," *J. Phys. Chem. B*, vol. 110, no. 43, pp. 21950–21957, 2006.

[6] C. S. Kiminami, "Primary crystallization in amorphous Al 84 Ni 8 Co 4 Y 3 Zr 1 alloy," *J. Non. Cryst. Solids*, vol. 304, pp. 36–43, 2002.

[7] M. Ovun, M. J. Kramer, and Y. E. Kalay, "Structural modeling of liquid and amorphous Al91Tb9 by Monte Carlo simulations," *J. Non. Cryst. Solids*, vol. 405, pp. 27–32, 2014.

[8] M. F. Ashby and a. L. Greer, "Metallic glasses as structural materials," *Scr. Mater.*, vol. 54, no. 3, pp. 321–326, 2006.

[9] M. F. Ashby and A. L. Greer, "Metallic glasses as structural materials," *Scr. Mater.*, vol. 54, no. 3, pp. 321–326, 2006.

[10] C. Suryanarayana and A. Inoue, *Bulk Metallic Glasses*. CRC Press, 2011.

[11] W. Kauzmann, "The Nature of the Glassy State and the Behavior of Liquids at Low Temperatures.," *Chem. Rev.*, vol. 43, no. 2, pp. 219–256, Oct. 1948.

[12] P. G. Debenedetti and F. H. Stillinger, "Supercooled liquids and the glass transition," *Nature*, vol. 410, no. 6825, pp. 259–267, 2001.

[13] H. Vogel, "Das temperatur-abhängigkeitsgesetz der viskosität von flüssigkeiten," *Phys. Zeit.*, vol. 22, pp. 645–646, 1921.

[14] G. Tammann and W. Hesse, "Die abhängigkeit der viskosität von der temperatur bei unterkühlten flüssigkeiten," *Z. Anorg. Allg. Chem.*, vol. 156, pp. 245–257, 1926.

[15] G. S. Fulcher, "Analysis of recent measurements of the viscosity of glasses," *J. Am. Ceram. Soc.*, vol. 8, p. 339, 1925.

[16] V. Lubchenko and P. G. Wolynes, "Theory of Structural Glasses and Supercooled Liquids," *Annu. Rev. Phys. Chem.*, vol. 58, no. 1, pp. 235–266,

2007.

[17] V. I. Kalikmanov, *Nucleation Theory*, vol. 860. 2013.

[18] P. E. Wagner and G. Vali, Eds., *Atmospheric Aerosols and Nucleation*, vol. 309. Berlin, Heidelberg: Springer Berlin Heidelberg, 1988.

[19] A. I. Zhmakin, *Fundamentals of cryobiology: Physical Phenomena and Mathematical Mode*. Springer, 2008.

[20] M. A. A. Schoonen, Y. Xu, and J. Bebie, "Energetics and Kinetics of the Prebiotic Synthesis of Simple Organic Acids and Amino Acids With the Fes-H 2 S/Fes 2 Redox Couple As Reductant," pp. 5–32, 1999.

[21] F. L. Sousa, T. Thiergart, G. Landan, S. Nelson-Sathi, I. a C. Pereira, J. F. Allen, N. Lane, and W. F. Martin, "Early bioenergetic evolution.," *Philos. Trans. R. Soc. Lond. B. Biol. Sci.*, vol. 368, no. 1622, p. 20130088, 2013.

[22] L. J. Rothschild and R. L. Mancinelli, "Life in extreme environments," *Nature*, vol. 409, no. September 2000, pp. 1092–1101, 2001.

[23] W. Callister and D. Rethwisch, *Materials science and engineering: an introduction*, vol. 94. 2007.

[24] E. Takeshi and S. J. L. Billinge, *Underneath the Bragg Peaks: Structural Analysis of Complex Materials*, vol. 16. 2012.

[25] S. R. Elliott, "Origin of the first sharp diffraction peak in the structure factor of covalent glasses," *Phys. Rev. Lett.*, vol. 67, no. 6, p. 711, 1991.

[26] S. R. Elliott, "The origin of the first sharp diffraction peak in the structure factor of covalent glasses and liquids," *J. Phys. Condens. Matter*, vol. 4, no. 38, p. 7661, 1992.

[27] H. W. Sheng, G. Wilde, and E. Ma, "The competing crystalline and amorphous solid solutions in the Ag–Cu system," *Acta Mater.*, vol. 50, no. 3, pp. 475–488, 2002.

[28] T. F. Kelly and M. K. Miller, "Atom probe tomography," *Rev. Sci. Instrum.*, vol. 78, no. 3, p. 31101, 2007.

[29] B. Gault, M. P. Moody, F. De Geuser, A. La Fontaine, L. T. Stephenson, D. Haley, and S. P. Ringer, "Spatial resolution in atom probe tomography.," *Microsc. Microanal.*, vol. 16, no. 1, pp. 99–110, 2010.

[30] Y. E. Kalay, L. S. Chumbley, and I. E. Anderson, "Crystallization behavior in a highly driven marginal glass forming alloy," *J. Non. Cryst. Solids*, vol. 354, no. 26, pp. 3040–3048, 2008.

[31] Y. E. Kalay, C. Yeager, L. S. Chumbley, M. J. Kramer, and I. E. Anderson, "Initial crystallization in a nanostructured Al-Sm rare earth alloy," *J. Non. Cryst. Solids*, vol. 356, no. 28–30, pp. 1416–1424, 2010.

[32] M. M. J. Treacy, J. M. Gibson, L. Fan, D. J. Paterson, and I. McNulty, "Fluctuation microscopy: a probe of medium range order," *Reports Prog. Phys.*,

vol. 68, no. 12, p. 2899, 2005.

[33] A. Tildeslay, “Computer Simulation of Liquids.” Oxford, 1991.

[34] D. C. C. Rapaport, *The Art of Molecular Dynamics Simulation*, vol. 2. 2004.

[35] A. Satoh, *Introduction to Practice of Molecular Simulation*. Elsevier Ltd, 2011.

[36] D. Frenkel and B. Smit, “Understanding Molecular Simulation: From Algorithms to Applications (Computational Science),” *... Princ. Pract. Monte Carlo Mol. ...*, p. 664, 2002.

[37] L. Verlet, “Computer‘ experiments’ on classical fluids. I. Thermodynamical properties of Lennard-Jones molecules,” *Phys. Rev.*, vol. 159, no. 1, p. 98, 1967.

[38] M. H. Kalos and P. A. Whitlock, *Monte carlo methods*. John Wiley & Sons, 2008.

[39] D. G. Luenberger, *Introduction to linear and nonlinear programming*, vol. 28. Addison-Wesley Reading, MA, 1973.

[40] R. Battiti, “First-and second-order methods for learning: between steepest descent and Newton’s method,” *Neural Comput.*, vol. 4, no. 2, pp. 141–166, 1992.

[41] N. Metropolis, A. W. Rosenbluth, M. N. Rosenbluth, A. H. Teller, and E. Teller, “Equation of state calculations by fast computing machines,” *J. Chem. Phys.*, vol. 21, no. 6, pp. 1087–1092, 1953.

[42] R. L. McGreevy and L. Pusztai, “Reverse Monte Carlo simulation: a new technique for the determination of disordered structures,” *Mol. Simul.*, vol. 1, no. 6, pp. 359–367, 1988.

[43] P. Biswas, R. Atta-Fynn, and D. A. Drabold, “Reverse Monte Carlo modeling of amorphous silicon,” *Phys. Rev. B*, vol. 69, no. 19, p. 195207, 2004.

[44] M. G. Tucker, D. A. Keen, M. T. Dove, and K. Trachenko, “Refinement of the Si–O–Si bond angle distribution in vitreous silica,” *J. Phys. Condens. Matter*, vol. 17, no. 5, p. S67, 2005.

[45] S. J. Gurman and R. L. McGreevy, “Reverse Monte Carlo simulation for the analysis of EXAFS data,” *J. Phys. Condens. Matter*, vol. 2, no. 48, p. 9463, 1990.

[46] P. Jóvári, S. N. Yannopoulos, I. Kaban, A. Kalampounias, I. Lishchynskyy, B. Beuneu, O. Kostadinova, E. Welter, and A. Schöps, “Structure of AsxTe100−x (20⩽ x⩽ 60) glasses investigated with x-ray absorption fine structure, x-ray and neutron diffraction, and reverse Monte Carlo simulation,” *J. Chem. Phys.*, vol. 129, no. 21, p. 214502, 2008.

[47] K. D. Machado, J. C. de Lima, A. A. M. Gasperini, S. M. Souza, C. E. Maurmann, R. G. Delaplane, and A. Wannberg, “X-ray and neutron diffraction studies and reverse Monte Carlo simulations of an amorphous Ni60Ti40 alloy produced by mechanical alloying,” *J. Phys. Condens. Matter*, vol. 17, no. 10, p. 1703, 2005.

[48] U. Hoppe, G. Walter, G. Carl, J. Neuefeind, and A. C. Hannon, “Structure of zinc phosphate glasses probed by neutron and X-ray diffraction of high resolving power and by reverse Monte Carlo simulations,” *J. Non. Cryst. Solids*, vol. 351, no. 12, pp. 1020–1031, 2005.

[49] T. X. Nguyen, N. Cohaut, J.-S. Bae, and S. K. Bhatia, “New method for atomistic modeling of the microstructure of activated carbons using hybrid reverse Monte Carlo simulation,” *Langmuir*, vol. 24, no. 15, pp. 7912–7922, 2008.

[50] S. K. Jain, R. J.-M. Pellenq, J. P. Pikunic, and K. E. Gubbins, “Molecular modeling of porous carbons using the hybrid reverse Monte Carlo method,” *Langmuir*, vol. 22, no. 24, pp. 9942–9948, 2006.

[51] T. X. Nguyen, S. K. Bhatia, S. K. Jain, and K. E. Gubbins, “Structure of saccharose-based carbon and transport of confined fluids: hybrid reverse Monte Carlo reconstruction and simulation studies,” *Mol. Simul.*, vol. 32, no. 7, pp. 567–577, 2006.

[52] G. Opletal, T. C. Petersen, D. G. McCulloch, I. K. Snook, and I. Yarovsky, “The structure of disordered carbon solids studied using a hybrid reverse Monte Carlo algorithm,” *J. Phys. Condens. Matter*, vol. 17, no. 17, p. 2605, 2005.

[53] G. Opletal, T. Petersen, B. O’Malley, I. Snook, D. G. McCulloch, N. A. Marks, and I. Yarovsky, “Hybrid approach for generating realistic amorphous carbon structure using metropolis and reverse Monte Carlo,” *Mol. Simul.*, vol. 28, no. 10–11, pp. 927–938, 2002.

[54] S. Fesciyan and H. L. Frisch, “An inverse problem in statistical mechanics,” *J. Math. Phys.*, vol. 16, no. 10, pp. 1989–1991, 1975.

[55] R. Evans, “Comment on reverse Monte Carlo simulation,” *Mol. Simul.*, vol. 4, no. 6, pp. 409–411, 1990.

[56] N. Almarza and E. Lomba, “Determination of the interaction potential from the pair distribution function: An inverse Monte Carlo technique,” *Phys. Rev. E*, vol. 68, no. 1, pp. 1–6, 2003.

[57] M. L. de Haro, A. Santos, and S. B. Yuste, “On the radial distribution function of a hard-sphere fluid,” *J. Chem. Phys.*, vol. 124, no. 23, p. 236102, 2006.

[58] R. L. Davidchack, “Hard spheres revisited: Accurate calculation of the solid–liquid interfacial free energy,” *J. Chem. Phys.*, vol. 133, no. 23, p. 234701, 2010.

[59] M. Isobe and W. Krauth, “Hard-sphere melting and crystallization with event-chain Monte Carlo,” *J. Chem. Phys.*, vol. 143, no. 8, p. 84509, 2015.

[60] D. B. Miracle, “A structural model for metallic glasses,” *Nat. Mater.*, vol. 3, no. 10, pp. 697–702, 2004.

[61] D. B. Miracle, “The efficient cluster packing model–An atomic structural model for metallic glasses,” *Acta Mater.*, vol. 54, no. 16, pp. 4317–4336, 2006.

[62] D. B. Miracle and P. Harrowell, “Noncrystalline compact packings of hard

spheres of two sizes: Bipyramids and the geometry of common neighbors.," *J. Chem. Phys.*, vol. 130, no. 11, p. 114505, 2009.

[63] J. E. Jones, "On the determination of molecular fields. II. From the equation of state of a gas," in *Proceedings of the Royal Society of London A: Mathematical, Physical and Engineering Sciences*, 1924, vol. 106, no. 738, pp. 463–477.

[64] R. A. Buckingham, "The classical equation of state of gaseous helium, neon and argon," in *Proceedings of the Royal Society of London A: Mathematical, Physical and Engineering Sciences*, 1938, vol. 168, no. 933, pp. 264–283.

[65] G. M. Torrie and J. P. Valleau, "Monte Carlo free energy estimates using non-Boltzmann sampling: application to the sub-critical Lennard-Jones fluid," *Chem. Phys. Lett.*, vol. 28, no. 4, pp. 578–581, 1974.

[66] J. J. Nicolas, K. E. Gubbins, W. B. Streett, and D. Tildesley, "Equation of state for the Lennard-Jones fluid," *Mol. Phys.*, vol. 37, no. 5, pp. 1429–1454, 1979.

[67] B. Smit, "Phase diagrams of Lennard-Jones fluids," *J. Chem. Phys.*, vol. 96, no. 11, pp. 8639–8640, 1992.

[68] J. Kolafa and I. Nezbeda, "The Lennard-Jones fluid: An accurate analytic and theoretically-based equation of state," *Fluid Phase Equilib.*, vol. 100, pp. 1–34, 1994.

[69] P. M. Morse, "Diatomic molecules according to the wave mechanics. II. vibrational levels," *Phys. Rev.*, vol. 34, no. 1, p. 57, 1929.

[70] J. P. Dahl and M. Springborg, "The Morse oscillator in position space, momentum space, and phase space," *J. Chem. Phys.*, vol. 88, no. 7, pp. 4535–4547, 1988.

[71] L. A. Girifalco and V. G. Weizer, "Application of the Morse potential function to cubic metals," *Phys. Rev.*, vol. 114, no. 3, p. 687, 1959.

[72] F. H. Stillinger and T. A. Weber, "Computer simulation of local order in condensed phases of silicon," *Phys. Rev. B*, vol. 31, no. 8, p. 5262, 1985.

[73] M. Ichimura, "Stillinger-Weber potentials for III–V compound semiconductors and their application to the critical thickness calculation for InAs/GaAs," *Phys. status solidi*, vol. 153, no. 2, pp. 431–437, 1996.

[74] M. Z. Bazant, E. Kaxiras, and J. F. Justo, "Environment-dependent interatomic potential for bulk silicon," *Phys. Rev. B*, vol. 56, no. 14, p. 8542, 1997.

[75] J. F. Justo, M. Z. Bazant, E. Kaxiras, V. V Bulatov, and S. Yip, "Interatomic potential for silicon defects and disordered phases," *Phys. Rev. B*, vol. 58, no. 5, p. 2539, 1998.

[76] M. S. Daw and M. I. Baskes, "Embedded-atom method: Derivation and application to impurities, surfaces, and other defects in metals," *Phys. Rev. B*, vol. 29, no. 12, p. 6443, 1984.

[77] G. M. Bhuiyan, M. Silbert, and M. J. Stott, "Structure and thermodynamic properties of liquid transition metals: An embedded-atom-method approach,"

Phys. Rev. B, vol. 53, no. 2, p. 636, 1996.

[78] S. M. Foiles, "Application of the embedded-atom method to liquid transition metals," *Phys. Rev. B*, vol. 32, no. 6, p. 3409, 1985.

[79] S. M. Foiles and J. B. Adams, "Thermodynamic properties of fcc transition metals as calculated with the embedded-atom method," *Phys. Rev. B*, vol. 40, no. 9, p. 5909, 1989.

[80] R. LeSar, R. Najafabadi, and D. J. Srolovitz, "Thermodynamics of solid and liquid embedded-atom-method metals: A variational study," *J. Chem. Phys.*, vol. 94, no. 7, pp. 5090–5097, 1991.

[81] J. Lu and J. A. Szpunar, "Applications of the embedded-atom method to glass formation and crystallization of liquid and glass transition-metal nickel," *Philos. Mag. A*, vol. 75, no. 4, pp. 1057–1066, 1997.

[82] J. Mei, J. W. Davenport, and G. W. Fernando, "Analytic embedded-atom potentials for fcc metals: Application to liquid and solid copper," *Phys. Rev. B*, vol. 43, no. 6, p. 4653, 1991.

[83] M. M. G. Alemany, C. Rey, and L. J. Gallego, "Computer simulation study of the dynamic properties of liquid Ni using the embedded-atom model," *Phys. Rev. B*, vol. 58, no. 2, p. 685, 1998.

[84] M. Asta, D. Morgan, J. J. Hoyt, B. Sadigh, J. D. Althoff, D. De Fontaine, and S. M. Foiles, "Embedded-atom-method study of structural, thermodynamic, and atomic-transport properties of liquid Ni-Al alloys," *Phys. Rev. B*, vol. 59, no. 22, p. 14271, 1999.

[85] M. I. Mendelev, J. Schmalian, C. Z. Wang, J. R. Morris, and K. M. Ho, "Interface mobility and the liquid-glass transition in a one-component system described by an embedded atom method potential," *Phys. Rev. B*, vol. 74, no. 10, p. 104206, 2006.

[86] F. Shimizu, S. Ogata, and J. Li, "Yield point of metallic glass," *Acta Mater.*, vol. 54, no. 16, pp. 4293–4298, 2006.

[87] J. Zhang, F. Ma, and K. Xu, "Calculation of the surface energy of bcc metals by using the modified embedded-atom method," *Surf. interface Anal.*, vol. 35, no. 8, pp. 662–666, 2003.

[88] P. L. Williams, Y. Mishin, and J. C. Hamilton, "An embedded-atom potential for the Cu–Ag system," *Model. Simul. Mater. Sci. Eng.*, vol. 14, no. 5, p. 817, 2006.

[89] "Interatomic Potentials Repository Project," 2016. [Online]. Available: http://www.ctcms.nist.gov/potentials/. [Accessed: 31-Jan-2016].

[90] T. Schlick, *Molecular modeling and simulation: an interdisciplinary guide: an interdisciplinary guide*, vol. 21. Springer Science & Business Media, 2010.

[91] O. N. de Souza and R. L. Ornstein, "Effect of periodic box size on aqueous molecular dynamics simulation of a DNA dodecamer with particle-mesh Ewald

method," *Biophys. J.*, vol. 72, no. 6, pp. 2395–2397, 1997.

[92] J. D. Honeycutt and H. C. Andersen, "The effect of periodic boundary conditions on homogeneous nucleation observed in computer simulations," *Chem. Phys. Lett.*, vol. 108, no. 6, pp. 535–538, 1984.

[93] M. J. Mandell, "On the properties of a periodic fluid," *J. Stat. Phys.*, vol. 15, no. 4, pp. 299–305, 1976.

[94] R. Serway and J. Jewett, *Principles of physics: a calculus-based text*, vol. 1. Nelson Education, 2012.

[95] S. Thompson, "Use of neighbor lists in molecular dynamics," *Inf. Quaterly, CCP5*, vol. 8, pp. 20–28, 1983.

[96] B. Quentrec and C. Brot, "New method for searching for neighbors in molecular dynamics computations," *J. Comput. Phys.*, vol. 13, no. 3, pp. 430–432, 1973.

[97] R. W. Hockney and J. W. Eastwood, *Computer simulation using particles*. CRC Press, 1988.

[98] T. Egami and S. J. L. Billinge, *Underneath the Bragg peaks: structural analysis of complex materials*, vol. 16. Elsevier, 2003.

[99] M. I. Mendelev, M. J. Kramer, R. T. Ott, D. J. Sordelet, D. Yagodin, and P. Popel, "Development of suitable interatomic potentials for simulation of liquid and amorphous Cu–Zr alloys," *Philos. Mag.*, vol. 89, no. 11, pp. 967–987, 2009.

[100] D. Y. Sun, M. I. Mendelev, C. A. Becker, K. Kudin, T. Haxhimali, M. Asta, J. J. Hoyt, A. Karma, and D. J. Srolovitz, "Crystal-melt interfacial free energies in hcp metals: A molecular dynamics study of Mg," *Phys. Rev. B*, vol. 73, no. 2, p. 24116, 2006.

[101] A. Bari, T. Das, and R. N. Joarder, "Effective pair potential and thermodynamics of liquid transition metals Fe, Co and Ni," *J. Non. Cryst. Solids*, vol. 136, no. 1, pp. 173–180, 1991.

[102] J. Jalkanen and M. H. Müser, "Systematic analysis and modification of embedded-atom potentials: case study of copper," *Model. Simul. Mater. Sci. Eng.*, vol. 23, no. 7, p. 74001, 2015.

[103] C. Rycroft, "Voro++: A three-dimensional Voronoi cell library in C++," *Lawrence Berkeley Natl. Lab.*, 2009.

[104] J. Hwang, Z. H. Melgarejo, Y. E. Kalay, I. Kalay, M. J. Kramer, D. S. Stone, and P. M. Voyles, "Nanoscale structure and structural relaxation in Zr50Cu45Al5 bulk metallic glass," *Phys. Rev. Lett.*, vol. 108, no. 19, pp. 1–5, 2012.

[105] A. S. Clarke and H. Jónsson, "Structural changes accompanying densification of random hard-sphere packings," *Phys. Rev. E*, vol. 47, no. 6, p. 3975, 1993.

[106] A. Stukowski, "Structure identification methods for atomistic simulations of crystalline materials," *Model. Simul. Mater. Sci. Eng.*, vol. 20, no. 4, p. 45021, 2012.

[107] J. D. Honeycutt and H. C. Andersen, “Molecular dynamics study of melting and freezing of small Lennard-Jones clusters,” *J. Phys. Chem.*, vol. 91, no. 19, pp. 4950–4963, 1987.

[108] W. Mickel, S. C. Kapfer, G. E. Schröder-Turk, and K. Mecke, “Shortcomings of the Bond Orientational Order Parameters for the Analysis of Disordered Particulate Matter,” *J. Chem. Phys.*, vol. 138, no. 4, pp. 1–8, Sep. 2012.

[109] B. E. Warren, *X-ray Diffraction*. Courier Corporation, 1969.

[110] J. M. Cowley, “X-ray measurement of order in single crystals of Cu3Au,” *J. Appl. Phys.*, vol. 21, no. 1, pp. 24–30, 1950.

[111] G. S. Cargill and F. Spaepen, “Description of chemical ordering in amorphous alloys,” *J. Non. Cryst. Solids*, vol. 43, no. 1, pp. 91–97, 1981.

[112] P. J. Steinhardt, D. R. Nelson, and M. Ronchetti, “Bond-orientational order in liquids and glasses,” *Phys. Rev. B*, vol. 28, no. 2, p. 784, 1983.

[113] H. Tanaka, “Importance of many-body orientational correlations in the physical description of liquids,” *Faraday Discuss.*, vol. 167, p. 9, Jan. 2013.

[114] H. Tanaka, “Bond orientational order in liquids: Towards a unified description of water-like anomalies, liquid-liquid transition, glass transition, and crystallization: Bond orientational order in liquids.,” *Eur. Phys. J. E. Soft Matter*, vol. 35, no. 10, p. 113, Oct. 2012.

[115] W. Lechner and C. Dellago, “Accurate determination of crystal structures based on averaged local bond order parameters,” *J. Chem. Phys.*, vol. 129, no. 11, p. 114707, 2008.

[116] A. Inoue, “Amorphous, nanoquasicrystalline and nanocrystalline alloys in Al-based systems,” *Prog. Mater. Sci.*, vol. 43, no. 5, pp. 365–520, 1998.

[117] J. H. Perepezko, R. J. Hebert, R. I. Wu, and G. Wilde, “Primary crystallization in amorphous Al-based alloys,” *J. Non. Cryst. Solids*, vol. 317, no. 1–2, pp. 52–61, 2003.

[118] T. Kulik, “Nanocrystallization of metallic glasses,” *J. Non. Cryst. Solids*, vol. 287, no. 1–3, pp. 145–161, 2001.

[119] L. Battezzati, S. Pozzovivo, and P. Rizzi, “Nanocrystalline aluminium alloys,” *Nanoclusters Nanocrystals, Am. Sci. Publ.*, vol. 25650, pp. 91381–91439, 2003.

[120] K. K. Sahu, N. a. Mauro, L. Longstreth-Spoor, D. Saha, Z. Nussinov, M. K. Miller, and K. F. Kelton, “Phase separation mediated devitrification of Al88Y7Fe5 glasses,” *Acta Mater.*, vol. 58, no. 12, pp. 4199–4206, 2010.

[121] G. Wilde, H. Sieber, and J. H. Perepezko, “Glass formation versus nanocrystallization in an Al92Sm8 alloy,” *Scr. Mater.*, vol. 40, no. 7, pp. 779–783, 1999.

[122] W. G. Stratton, J. Hamann, J. H. Perepezko, P. M. Voyles, X. Mao, and S. V. Khare, “Aluminum nanoscale order in amorphous Al92 Sm8 measured by fluctuation electron microscopy,” *Appl. Phys. Lett.*, vol. 86, no. 14, pp. 1–3,

2005.

[123] a. K. Gangopadhyay, T. K. Croat, and K. F. Kelton, “Effect of phase separation on subsequent crystallization in Al88Gd6La2Ni4,” *Acta Mater.*, vol. 48, no. 16, pp. 4035–4043, 2000.

[124] K. F. Kelton, “Time-dependent nucleation in partitioning transformations,” *Acta Mater.*, vol. 48, no. 8, pp. 1967–1980, 2000.

[125] Y. E. Kalay, L. S. Chumbley, and I. E. Anderson, “Characterization of a marginal glass former alloy solidified in gas atomized powders,” *Mater. Sci. Eng. A*, vol. 490, no. 1–2, pp. 72–80, Aug. 2008.

[126] Y. E. Kalay, I. Kalay, J. Hwang, P. M. Voyles, and M. J. Kramer, “Local chemical and topological order in Al–Tb and its role in controlling nanocrystal formation,” *Acta Mater.*, 2012.

[127] N. Tian, M. Ohnuma, T. Ohkubo, and K. Hono, “Primary crystallization of an Al88Gd6Er2Ni4 metallic glass,” *Mater. Trans.*, vol. 46, no. 12, pp. 2880–2885, 2005.

[128] Q. Li, E. Johnson, A. Johansen, and L. Sarholt-Kristensen, “On glass formation in rapidly solidified aluminum-based alloys,” *J. Mater. Res.*, vol. 7, no. 10, pp. 2756–2764, 1992.

[129] Y. E. Kalay, L. S. Chumbley, M. J. Kramer, and I. E. Anderson, “Local structure in marginal glass forming Al--Sm alloy,” *Intermetallics*, vol. 18, no. 8, pp. 1676–1682, 2010.

[130] N. Mattern, T. Gemming, J. Thomas, G. Goerigk, H. Franz, and J. Eckert, “Phase separation in Ni-Nb-Y metallic glasses,” *J. Alloys Compd.*, vol. 495, no. 2, pp. 299–304, 2010.

[131] J. Antonowicz, “Atomic packing and phase separation in Al-rare earth metallic glasses,” *J. Mater. Sci.*, vol. 45, no. 18, pp. 5040–5044, 2010.

[132] J. Antonowicz, “Phase separation and nanocrystal formation in Al-based metallic glasses,” *J. Alloys Compd.*, vol. 434–435, no. SPEC. ISS., pp. 126–130, 2007.

[133] J. Antonowicz, E. Jezierska, M. Kedzierski, A. R. Yavari, L. Greer, P. Panine, and M. Sztucki, “Early stages of phase separation and nanocrystallization in Al-rare earth metallic glasses studied using SAXS/WAXS and HRTEM methods,” *Rev. Adv. Mater. Sci.*, vol. 18, no. 5, pp. 454–458, 2008.

[134] G. Kresse and J. Furthmüller, “Efficiency of ab-initio total energy calculations for metals and semiconductors using a plane-wave basis set,” *Comput. Mater. Sci.*, vol. 6, no. 1, pp. 15–50, 1996.

[135] G. Kresse, “Efficient iterative schemes for ab initio total-energy calculations using a plane-wave basis set,” *Phys. Rev. B*, vol. 54, no. 16, pp. 11169–11186, 1996.

[136] G. Kresse and J. Hafner, “Ab initio molecular dynamics for liquid metals,”

Phys. Rev. B, vol. 47, no. 1, 1993.

[137] G. Kresse, "From ultrasoft pseudopotentials to the projector augmented-wave method," *Phys. Rev. B*, vol. 59, no. 3, pp. 1758–1775, 1999.

[138] R. L. McGreevy, "Reverse Monte Carlo modelling," *J. Phys. Condens. Matter*, vol. 13, no. 46, pp. R877–R913, 2001.

[139] M. I. Mendelev, M. J. Kramer, S. G. Hao, K. M. Ho, and C. Z. Wang, "Development of interatomic potentials appropriate for simulation of liquid and glass properties of NiZr2 alloy," *Philos. Mag.*, no. August 2015, pp. 1–16, 2012.

[140] Q. Jingyu, B. Xiufang, S. I. Sliusarenko, and W. Weimin, "Pre-peak in the structure factor of liquid Al-Fe alloy," *J. Phys. Condens. Matter*, vol. 10, no. 6, pp. 1211–1218, Feb. 1998.

[141] F. C. Frank, "Supercooling of Liquids," *Proc. R. Soc. Lond. A. Math. Phys. Sci.*, vol. 215, no. 1120, pp. 43–46 CR – Copyright © 1952 The Royal Societ, Nov. 1952.

[142] D. R. Allen, J. C. Foley, and J. H. Perepezko, "Nanocrystal development during primary crystallization of amorphous alloys," *Acta Mater.*, vol. 46, no. 2, pp. 431–440, 1998.

[143] Y. Q. Cheng, H. W. Sheng, and E. Ma, "Relationship between structure, dynamics, and mechanical properties in metallic glass-forming alloys," *Phys. Rev. B - Condens. Matter Mater. Phys.*, vol. 78, no. 1, pp. 1–7, 2008.

[144] A. F. Wallace, L. O. Hedges, A. Fernandez-martinez, P. Raiteri, J. D. Gale, G. a Waychunas, S. Whitelam, J. F. Banfield, and J. J. De Yoreo, "Supersaturated CaCO 3 Solutions," vol. 341, no. August, pp. 689–692, 2013.

[145] T. Demirtaş and Y. E. Kalay, "Kinetics of fcc-Al nanocrystallization in Al90Tb10 metallic glass," *J. Non. Cryst. Solids*, vol. 378, pp. 71–78, Oct. 2013.

[146] M. I. Mendelev, F. Zhang, Z. Ye, Y. Sun, M. C. Nguyen, S. R. Wilson, C. Z. Wang, and K. M. Ho, "Development of interatomic potentials appropriate for simulation of devitrification of Al90Sm10 alloy," *Model. Simul. Mater. Sci. Eng.*, vol. 23, no. 4, p. 45013, 2015.

[147] P. R. ten Wolde, M. J. Ruiz-Montero, and D. Frenkel, "Numerical calculation of the rate of crystal nucleation in a Lennard-Jones system at moderate undercooling," *J. Chem. Phys.*, vol. 104, no. 24, pp. 9932–9947, 1996.

[148] M. Övün. (2016, 30 June) "AmorphSim". [Online]. Available: https://github.com/mertovun/AmorphSim